Quaternary Science Reviews 256 (2021) 106833

Contents lists available at ScienceDirect

Quaternary Science Reviews

journal homepage: www.elsevier.com/locate/quascirev

# Atlantic water inflow to Labrador Sea and its interaction with ice sheet dynamics during the Holocene

Jens Weiser [a, *], Jürgen Titschack [a, f], Markus Kienast [b], Ian Nicholas McCave [c], Annalena Antonia Lochte [d, e], Jeetendra Saini [g], Rüdiger Stein [a, g], Dierk Hebbeln [a]

[a] MARUM - Centre for Marine Environmental Science, University of Bremen, D-28359, Bremen, Germany
[b] Department of Oceanography, Dalhousie University, Halifax, B3H 4R2, Canada
[c] Godwin Laboratory for Palaeoclimate Research, Department of Earth Sciences, University of Cambridge, Cambridge, CB2 3EQ, UK
[d] Institute of Geosciences, Kiel University, Ludewig-Meyn-Straße 10, D-24118, Kiel, Germany
[e] GEOMAR Helmholtz Centre for Ocean Research Kiel, Wischhofstraße 1-3, D-24148, Kiel, Germany
[f] Senckenberg Am Meer, Abteilung für Meeresforschung, D-26382, Wilhelmshaven, Germany
[g] Alfred Wegener Institute Helmholtz Centre for Polar and Marine Research, D-27568, Bremerhaven, Germany

ARTICLE INFO

*Article history:*
Received 19 October 2020
Received in revised form
28 January 2021
Accepted 28 January 2021
Available online xxx

Handling Editor: A. Voelker

*Keywords:*
Sortable Silt
Current-speed reconstructions
AMOC
8.2-ka event
Greenland Ice Sheet
Labrador Sea
Baffin Bay

ABSTRACT

The hydrodynamics of the Labrador Sea, controlled by the complex interplay of oceanographic, atmospheric and ice-sheet processes, play a crucial role for the Atlantic Meridional Overturning Circulation (AMOC). An improved understanding of the hydrodynamics and its forcing in the past could therefore hold a key to understanding its future behaviour. At present, there is a remarkable temporal mismatch, in that the largely microfossil-based reconstructions of Holocene Atlantic-water inflow/influence in the Labrador Sea and Baffin Bay appear to lag grain size-based current strength reconstructions from the adjacent North Atlantic by > 2ka. Here, we present the first current strength record from the West Greenland shelf off Nuuk to reconstruct Atlantic Water (AW)-inflow to the Labrador Sea via the West Greenland Current. Our data show that the Holocene AW-inflow into Labrador Sea is well aligned with the Holocene Speed Maximum documented in the North Atlantic (McCave and Andrews, 2019; Quat. Sci. Rev. 223), suggesting a close coupling with the AMOC. The observed lag between the microfossil-based records and the Holocene Speed Maximum can be explained when considering the presence of an extended meltwater lens that prevented the shoaling of the inflowing Atlantic waters. Once the meltwater discharge waned after the cessation of large-scale melting of the surrounding ice sheets, the AW could influence the surface waters, independently of the strength of its inflow. Only then was an effective ocean-atmosphere heat transfer enabled, triggering the comparably late onset of the regional Holocene Thermal Maximum. Furthermore, sediment geochemical analyses show that short term cooling events, such as the 8.2 ka event related to the final drainage of glacial Lake Agassiz, lead to glacier advances of the Greenland Ice Sheet. Since the grain size data show that these events had no influence on the AW-inflow to the north eastern Labrador Sea, these advances must have been caused by atmospheric cooling. Consequently, we argue that (i) in this region, surface water-based proxies register AW *influence* rather than *inflow* (ii) the AW inflow into the Labrador Sea is controlled by the AMOC, but (iii) its impact on an effective ocean-atmosphere heat transfer was hindered by a prevailing meltwater lens in the early Holocene, i.e. until the cessation of large-scale melting of the surrounding ice sheets.



## 1. Introduction

Two of the major components in the Earth's climate system, the Atlantic meridional overturning circulation (AMOC) and the northern hemisphere ice sheets, interact in the northern North Atlantic surrounding Greenland (Duplessy et al., 1992; Hebbeln et al., 1998; Koç et al., 1996; Stein, 2008). While the ocean currents are important transporters of heat, energy, nutrients and carbon, acting at various depths (Ganachaud and Wunsch, 2000; Kuhlbrodt et al., 2007; Rahmstorf, 1996; Rahmstorf et al., 2005;

* Corresponding author.
*E-mail addresses:* jweiser@marum.de, jweiser@uni-bremen.de (J. Weiser).

https://doi.org/10.1016/j.quascirev.2021.106833

Schmittner, 2005), the importance of the ice sheets lies in their ability to store large amounts of freshwater during glacial as well as releasing these under warming climates (Lynch-Stieglitz et al., 2007; Vinther et al., 2009). Both are closely interlinked as a strong AMOC can provide the moisture needed for the growth of an ice sheet (Hebbeln et al., 1994; Johannessen et al., 2005), while the AMOC itself reacts sensitively to meltwater input from decaying ice sheets (Bakker et al., 2012; Böning et al., 2016; Driesschaert et al., 2007; Weijer et al., 2012).

One area of particular importance here is the Labrador Sea, which is one of the two major sites for deep-water formation in the North Atlantic, thereby forming one of the nodes of the AMOC (Buckley and Marshall, 2016; Yashayaev, 2007). During the last glacial as well as over the course of the Holocene, it bordered on both the Laurentide and Greenland ice sheets (LIS/GrIS, respectively), making it a hotspot for potential ice-ocean interaction (Dickson et al., 1996; Thornalley et al., 2018). Palaeoclimate reconstructions have shown that a catastrophic meltwater outbursts from an ice sheet into the Labrador Sea, such as the "8.2 ka event", can significantly perturb the AMOC and result in a pronounced cold-spell, recorded throughout the northern hemisphere (Alley and Ágústsdóttir, 2005; Bamberg et al., 2010; Ellison, 2006; Hillaire-Marcel et al., 2007; Kleiven et al., 2008; Renssen et al., 2001), highlighting the far-reaching effects of environmental perturbations in the Labrador Sea.

One of the main controls acting on the efficiency of the AMOC to transport heat and energy is the speed at which the involved currents (deep, intermediate or shallow) flow. Past current speeds can be reconstructed using grain-size analyses of marine deposits. In particular, the sortable silt mean grain size has been shown to react sensitively to current speed changes and subsequently developed as current-speed proxy (McCave et al, 1995, 2017; McCave and Hall, 2006). Within the North Atlantic, current-speed reconstructions using this proxy showed a distinct early Holocene Speed Maximum within surface currents (HSM; McCave and Andrews (2019b; 2019a)), as well as in the deep-water Iceland-Scotland Overflow Water (ISOW) (Thornalley et al., 2013) – both parts of the AMOC. Similarly, modelling studies suggest a HSM for the AMOC as a whole (Ritz et al., 2013). Within the Labrador Sea and Baffin Bay, the West Greenland Current (WGC), flowing north along the coast of western Greenland, is the main carrier of relatively warm and saline water from the North Atlantic. Indirect reconstructions of its strength, mainly based on microfossil analyses, however, suggest a delay in Atlantic water (AW)-inflow with respect to the HSM in the North Atlantic (Caron et al., 2019; Gibb et al., 2015; Hansen et al., 2020; Moros et al., 2016; Ouellet-Bernier et al., 2014). Yet another delay becomes apparent when comparing these timings to the regionally varying time frames of the Holocene Thermal Maximum (HTM), i.e. a period in the early to mid-Holocene when temperatures were higher than today (cf. Kaufman et al., 2004).

With this study, we aim at directly reconstructing the history of the shallow-water AW-inflow to the Labrador Sea to elucidate (i) the apparent delay of strengthened AW-inflow to the Labrador Sea and Baffin Bay in relation to the HSM in the North Atlantic and its potential impacts on regional ice-ocean-atmosphere interaction; as well as (ii) the reaction of the local hydrography to short-term coolings/meltwater inputs in the Holocene and potential linkages with GrIS-dynamics since, so far, no conclusive eastern Labrador Sea records of the 8.2 ka-event exist despite the proximity of the inferred location of meltwater injection.

### 1.1. Regional setting and modern hydrography

The physiography of the SW-Greenland shelf is characterized by an alternation of shallow (~150 m) platforms and significantly deeper (>500 m) troughs. The troughs cross the shelf nearly perpendicular to the coast and are usually connected to inshore fjord systems. Many of them are over-deepened (Batchelor and Dowdeswell, 2014; Slabon et al., 2016), meaning that the inner shelf trough can be significantly deeper than the outer shelf. These troughs were formed by the repeated advance and retreat of ice streams, which have led to both excavation and delivery of sediments during glacial-interglacial cycles (Batchelor et al., 2018; Batchelor and Dowdeswell, 2014; Dowdeswell et al., 2014; Ó Cofaigh et al., 2013).

The modern hydrography within the Labrador Sea is characterized by an anticlockwise circulation of two opposing current regimes. In the east, relatively warm and saline waters enter the Labrador Sea from the south via the West Greenland Current (WGC). The WGC itself represents a mixture of Atlantic waters originating from the Irminger Current (IC) and colder, less saline Arctic outflow waters carried by the East Greenland Current (EGC). Despite the partial mixing of EGC- and IC-waters, the water column within the WGC is usually well stratified, with a thin layer of cold and relatively fresh water overlaying the warmer and saltier core of the WGC in depths between 100 and 800 m. Flowing north, these waters eventually reach the shoals of southern Davis Strait, where the WGC is partially retroflected and partially continues north towards Baffin Bay. The retroflected portion eventually joins the second predominant surface current, the Labrador Current. This is the continuation of the Baffin Current, mainly transporting cold, low salinity Arctic outflow waters from the central Arctic and Canadian Arctic Archipelago through Labrador Sea into the North Atlantic (Buch, 2002; Cuny et al., 2005; Myers et al., 2007; Ribergaard, 2014; Tang et al., 2004).

## 2. Material and methods

Gravity core GeoB19905-1 (Pos.: 64° 21.68′ N; 52° 57.70' W, length: 1036 cm) was raised from the north-eastern Labrador Sea shelf from 483 m water depth during RV Maria S. Merian expedition MSM44 in 2015 (Fig. 1). The core site is located approximately 40 km off the coast within the Sukkertop trough, one of the prominent cross-shelf troughs. The visual core description and colour measurements show a rather homogenous composition of mainly olive grey muds (Dorschel et al., 2015).

### 2.1. Stratigraphy

The chronostratigraphy of core GeoB19905-1 is based on twelve Accelerator Mass Spectrometry (AMS) $^{14}$C-datings of 0.6–4 mg of mixed benthic foraminifera from the >100 μm fraction. The measurements were performed directly on the $CO_2$ gas with the MICADAS (Mini Carbon Dating System) at the Alfred Wegener Institute in Bremerhaven, Germany (for methodological details see (Wacker et al., 2013)).

The age model was constructed using a combination of the PaleoDataView-program (Langner and Mulitza, 2019) and the open source software package BACON (Blaauw and Christen, 2011, 2018). PaleoDataView (PDV) uses modelled reservoir ages (Butzin et al., 2017) to calibrate radiocarbon ages against IntCal13 (Reimer et al., 2013). The appropriate reservoir ages are chosen automatically based on the sample's radiocarbon age and location of the core. These reservoir ages, ranging from 866 to 1098 a, were subsequently used to construct the final age model with BACON. These reservoir ages are higher than those previously used in the region (e.g. calibration against *Marine13* that considers Holocene reservoir ages between 265 and 508 yrs (Heaton et al., 2020) with additional, local corrections of 140 ± 35 yrs; e.g., Jackson et al., 2017; Jennings et al., 2014; Ouellet-Bernier et al., 2014). However, according to

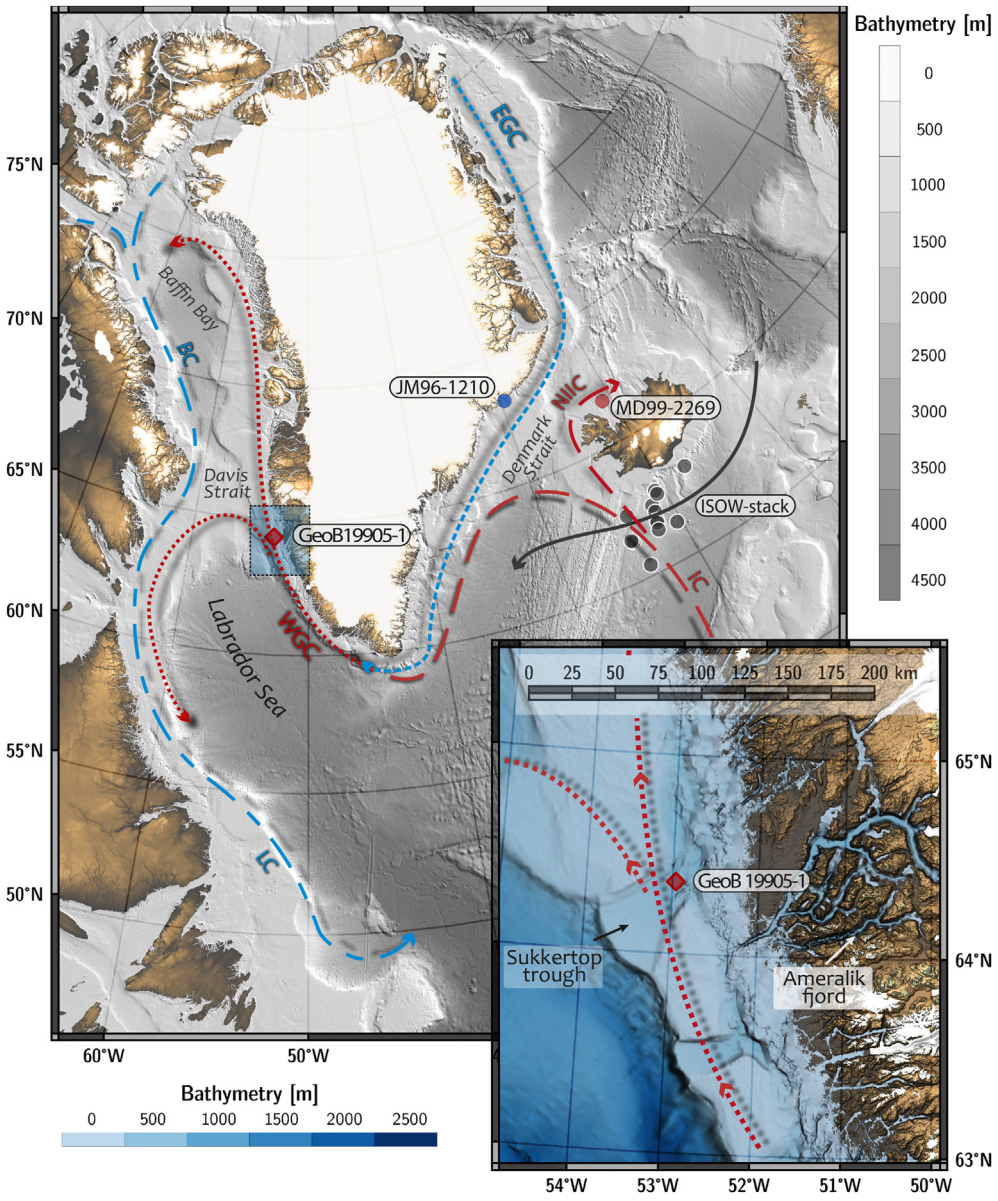


**Fig. 1.** Maps of the study area. Top left: overview of relevant hydrography and sites mentioned in the text. Dashed lines: surface currents with red lines indicating warmer, blue lines indicating cooler waters; solid line: deep water Iceland Scotland Overflow (ISOW). Red diamond: location of GeoB19905-1, other sediment core sites mentioned in the text are colored according to the main current they are influenced by. Top right: detailed map of the SW Greenland shelf with the location of the studied core in the Sukkertop trough. WGC: West Greenland Current, BC: Baffin Current, LC: Labrador Current, IC: Irminger Current, NIIC: North Iceland Irminger Current, EGC: East Greenland Current. Map data: GEBCO (GEBCO Compilation Group, 2020), IBCAOv4 (Jakobsson et al., 2020), TanDEM-X (German Aerospace Center (DLR), 2018), BedMachine v3 (Morlighem et al., 2017). (For interpretation of the references to colour in this figure legend, the reader is referred to the Web version of this article.)

Heaton et al. (2020), the global *marine calibration curves* are not suited for calibrating $^{14}C$ ages obtained from polar regions as these calibrations do not consider local effects of sea-ice, wind-stress and freshwater fluxes impacting on the oceanic $^{14}CO_2$ uptake. Therefore, the usage of modelled reservoir ages, as those provided by Butzin et al. (2017) considering theses aspects, are suggested for calibrating $^{14}C$ ages from polar regions (Heaton et al., 2020).

For the calculation of accumulation rates, sediment dry bulk density was assessed at 5–10 cm resolution, by weighing 10 $cm^3$ syringe samples prior to and after freeze-drying. The siliciclastic accumulation rates reported for grain-size end-members were acquired by subtracting the carbonate accumulation from bulk accumulation rates and multiplying that with the relative contribution of the respective end members. Carbonate concentrations are based on total carbon (TC) measurements (Carbon–Nitrogen–Sulfur Analyzer *Elementar-III, Vario)* and total organic carbon (TOC) measurements (Carbon–Sulfur Analyzer (*CS-800, ELTRA*) after carbonate removal with hydrochloric acid (37%, 500 μl)), performed at the Alfred-Wegener Institute, Bremerhaven. Assuming that the predominant carbonate phase is calcite and using a stoichiometric calculation factor of 8.333, carbonate contents were calculated as $CaCO_3$ [%] = (TC [%] − TOC [%])*8.333.

### 2.2. Granulometry

The disaggregated inorganic grain size distributions were determined in the Particle-Size Laboratory at MARUM, University of Bremen, with a Beckman Coulter Laser Diffraction Particle Size

Analyzer LS 13320, according to the following protocol (see also McGregor et al. (2009)): Prior to the measurements, the siliciclastic sediment fractions were isolated by removing organic carbon, calcium carbonate, and biogenic silica by boiling the samples (in about 200 ml water) with 10 ml of $H_2O_2$ (35%; until the reaction stopped), 10 ml of HCl (10%; 1 min) and 6 g NaOH pellets (10 min), respectively. After every preparation step, the samples were diluted (dilution factor: >25). Finally, remaining aggregates were destroyed prior to the measurements by boiling the samples with ~0.3 g tetrasodium diphosphate decahydrate ($Na_4P_2O_7$ * $10H_2O$, 3 min). Sample preparation and measurements were carried out with deionized, degassed and filtered water (filter mesh size: 0.2 μm) to reduce the potential influence of gas bubbles or particles within the water. The results provide the grain-size distribution of a sample from 0.04 to 2000 μm, divided into 116 size classes. The calculation of the grain sizes relies on the Fraunhofer diffraction theory and the Polarization Intensity Differential Scattering (PIDS) for particles from 0.4 to 2000 μm and from 0.04 to 0.4 μm, respectively. The reproducibility is checked regularly by replicate analyses of three internal glass-bead standards and is found to be better than ±0.7 μm for the mean and ±0.6 μm for the median particle size (1σ). The average standard deviation integrated over all size classes is better than ±4 vol% (note that the standard deviation of the individual size classes is not distributed uniformly).

Sortable silt mean grain size ($\overline{SS}$) was calculated following the protocol proposed by McCave and Andrews (2019b) outlining the applicability of laser scanner-derived grain-size data for sortable silt calculations. Modes were determined by using GRADISTATv9.1 (Blott and Pye, 2001) and subsequently classified into a fine (<12 μm), a medium (not used/shown) and a coarse (>38 μm) mode.

### 2.3. End member analysis (EMA)

Statistical unmixing of the grain-size data was performed using the MATLAB- software package *AnalySize* (Paterson and Heslop, 2015). We applied a non-parametric unmixing approach, where the end members (EMs) are estimated from the data itself (Chen and Guillaume, 2012) that is able to represent 98.5% of the dataset's variance by varying abundance of two genetically meaningful (cf. van Hateren et al., 2018) end-members ($r^2$ = 0.9848, EM-$r^2$ = 0.0033).

### 2.4. X-ray fluorescence (XRF)

XRF Core Scanner data were collected every one to 2 cm downcore over an active area of 15 $mm^2$ with a downcore slit size of 10 mm using generator settings of 10 and 30 kV directly at the split core surface of the archive half with XRF Core Scanner II (AVAATECH Serial No. 2) at MARUM, Bremen. The split core surface was covered with a 4 μm thin SPEX Certi Prep Ultralene foil to avoid contamination of the measuring unit and desiccation of the sediment. Raw results were processed by the analysis of X-Ray spectra with the Iterative Least Squares software package (WIN AXIL) by Canberra Eurisys. While a total of 25 elements were measured during the XRF scanning, a number of these were deemed unreliable due to low counts (Ni, Cu, Zn, Ga, Y, Nb, Mo, Bi, P, Cr, S) or interferences (Cl, Rh). Ca and Sr were removed to exclude influences of biogenically produced carbonates. Thus, the remaining dataset includes 11 elements: Al, Si, P, K, Ti, Mn, Fe, Br, Rb, Zr, Pb. Given that XRF scanning is a semiquantitative measurement, the individual element counts were normalised by division with the sum of all counts per sample to improve comparability and minimize effects from varying porosity, grain size or water content (Bahr et al., 2014; Boxberg et al., 2020; Lyle et al., 2012; Tjallingii et al., 2007; Weltje and Tjallingii, 2008). The data are accordingly reported as counts/total counts. For the purpose of this study, we focus on four of the main, terrestrially sourced elements: Al, Si, Fe, and Ti.

## 3. Results

### 3.1. Age model

The chronostratigraphy of core GeoB19905-1 is based on 12 AMS $^{14}C$ datings of mixed benthic foraminifera (Table 1). For the Bayesian age-depth model, two measurements were excluded: (i) the sample from 603 cm had to be measured twice, because of server-connectivity issues during the first measurement (AWI ID 1465.1.1, see Table 1) and although the 95% confidence intervals (CIs) of the calibrated ages from both measurements overlap, we excluded the first, possibly erroneous measurement, from the age modelling and only considered the second measurement; (ii) the data point at 505 cm was excluded because it revealed a much older age than the underlying samples (Fig. 2). Assuming a continuous sedimentation based on these radiocarbon dates would result in very low accumulation rates between 8.2 ka BP and 5.3 ka BP, leading to a significant reduction in the carbonate and foraminifera accumulation rate while the foraminifera contents in the sediment remain as high as before and after (see Supplement and Fig. S1). This mismatch can be resolved by assuming a hiatus, allowing to link the two parameters again. Further observations revealed a superordinate reduction in dry bulk density of ~0.4 g $cm^{-3}$ between 540 and 700 cm that separates older, more consolidated from younger less consolidated sediments. Two short-lived reductions in dry bulk density (~0.2 g $cm^{-3}$) at 640 and 670 cm core depth indicate presence of one or even two hiati (Fig. 2). However, at a core depth of 640 cm such a reduction is accompanied by a shift in the granulometric composition of the sediment at the same level, which is most prominent in the coarse mode (see below). Consequently, we place the hiatus at this level, although we cannot ultimately exclude that the hiatus, or in fact a second hiatus, is present at another depth within the aforementioned interval (for more details see the supplement). Nevertheless, placing the hiatus at 640 cm or at 670 cm core depth (or even two hiati at both depths) would not affect the overall interpretation of the data (see below).

Based on a hiatus at 640 cm depth, the resulting age model suggests a rather continuous sedimentation from 11.6 ka BP to 7.6 ka BP and since 5.9 ka BP. Thus, the hiatus at 640 cm core depth represents an interval of ~1.7 ka that partly overlaps with a hiatus identified in the nearby Ameralik Fjord that lasted from 6.8 to 4.4 ka BP (Ren et al., 2009).

Sedimentation rates of core GeoB19905-1 range from 80 to 120 cm $ka^{-1}$ (Fig. 2) for the majority of the Holocene, while a strong increase to >250 cm $ka^{-1}$ is recorded after 1.5 ka BP. Highest sediment accumulation rates (>125 g $cm^{-2}$ $ka^{-1}$) are recorded during the Deglacial until 9 ka BP and during the last 1.5 ka.

### 3.2. Granulometry

In general, the siliciclastic sediment fraction of core GeoB19905-1 can be classified as muddy to sandy silt (Fig. 3). While no material >250 μm was observed, the core shows an overall fining-upward trend (Fig. 4). Results from the EMA exhibit two EMs representing 98.5% of the data (Fig. 3). EM 1 shows a medium to poorly sorted, polymodal, meso-to platykurtic distribution centred around an overall modal grain size of approximately 10 μm. EM 2 is a well sorted, unimodal, leptokurtic sediment with a strong fine (negative) skew and a modal grain size of ~60 μm (Fig. 3).

**Table 1**
Results of the AMS-dating, calibration and Bayesion age modelling. Reservoir ages are in respect to IntCal13, min. And max. Ages correspond to the 5% & 95% confidence interval defined by PaleoDataView. Last column denotes ages after modelling with BACON.

| AMS-dating, MICADAS, AWI Bremerhaven | | | | Reservoir Correction and Calibration, PaleoDataView | | | | Modelling, BACON |
|---|---|---|---|---|---|---|---|---|
| Lab ID: AWI- | Depth [cm] | $^{14}$C-age [yrs.] | $^{14}$C-error [yrs.] | Reservoir age [yrs.] | Min. Age [cal. yrs. BP] | Max. Age [cal. yrs. BP] | Weighted mean age [cal. yrs. BP] | Weighted mean age [cal. yrs. BP] |
| 1462.1.1 | 48 | 1021 | 177 | 994 ± 53 | 0 | 455 | 178 | 210 |
| 1918.1.1 | 153 | 1678 | 109 | 1098 ± 51 | 318 | 741 | 575 | 742 |
| 1463.1.1 | 248 | 2036 | 184 | 988 ± 53 | 664 | 1311 | 982 | 1418 |
| 1916.1.1 | 323 | 3050 | 112 | 956 ± 52 | 1745 | 2352 | 2088 | 2158 |
| 1917.1.1 | 423 | 4054 | 114 | 956 ± 53 | 2959 | 3583 | 3283 | 3305 |
| 1464.1.1 | 505 | 6998 | 185 | 1015 ± 56 | 7425 | 8168 | 7765 | excluded |
| 1465.2.1 | 603 | 5671 | 76 | 1048 ± 51 | 5046 | 5583 | 5329 | 5468 |
| 1465.1.1 | 603 | 5246 | 191 | 933 ± 57 | 4413 | 5566 | 4922 | excluded |
| 4642.1.1 | 688 | 8422 | 88 | 999 ± 59 | 8022 | 8404 | 8232 | 8198 |
| 4643.1.1 | 708 | 8555 | 92 | 915 ± 65 | 8185 | 8683 | 8441 | 8406 |
| 1466.1.1 | 753 | 8946 | 187 | 994 ± 63 | 8404 | 9396 | 8838 | 8831 |
| 1467.1.1 | 953 | 10,263 | 191 | 866 ± 200 | 9894 | 11,597 | 10,692 | 10,752 |

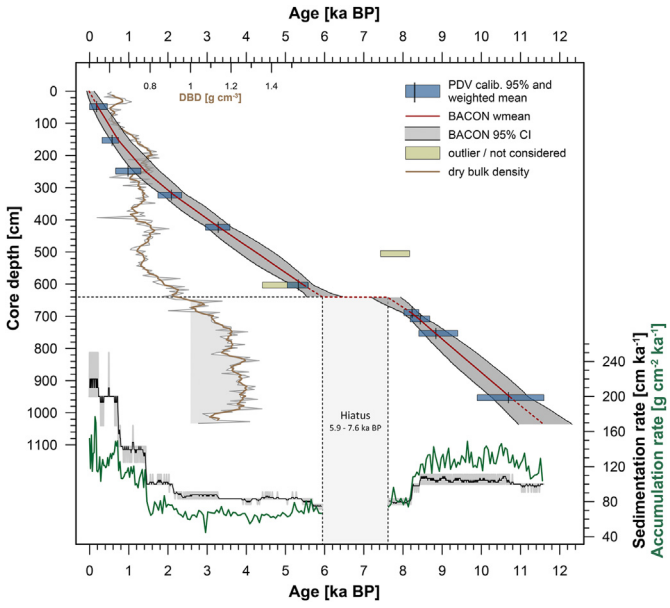


**Fig. 2.** Bayesian age-depth model for core GeoB19905-1. Rectangles denote the results of the radiocarbon dating (blue = valid, olive = outlier/not considered) and calibration (PDV: PaleoDataView) with the 95% confidence interval; red line marks the most likely age and the grey shading indicates the extend of the 95% confidence interval as determined by BACON. Intervals of less robust age control are stippled. Dry bulk density, including a 5-point running-average in brown, is shown on the left. In the bottom panel, the derived sedimentation rate (grey, 5 pt. average in black) and the bulk accumulation rate (green) are shown. (For interpretation of the references to colour in this figure legend, the reader is referred to the Web version of this article.)

Notwithstanding the fining-upward trend, the core can be divided into three intervals based on the respective grain-size distributions (GSDs) (Fig. 4b–d). During the early Holocene (11.6–7.6 ka BP), the GSDs are almost exclusively unimodal with a strong fine skew. The grain size of the coarse mode shows overall highest values of >50 μm, while the fine mode can only be determined rarely. Accordingly, this interval is dominated by EM2, which, on average, contributes 76 vol% to the sediment. The $\overline{SS}$ record shows highest values (>28 μm) in this interval. Only the basal part prior to 11 ka BP shows slightly finer $\overline{SS}$.

After the hiatus, i.e. during the mid-Holocene (5.9–2.2 ka BP), the GSDs maintain the fine skew but become increasingly polymodal, which also is reflected in an increased content of fine silt and clay. The coarse mode exhibits small grain sizes (~40 μm) until 5 ka BP, followed by a slight coarsening. From 5.9 ka BP onwards, the fine mode (~6–8 μm) is detected consistently in the sediment (Fig. 4f–g). Both EMs contribute approximately 50 vol% to the siliciclastic sediment fraction during this interval (Fig. 4e). Compared to the early Holocene, $\overline{SS}$ values decrease towards ~26 μm and remain stable until ~3.3 ka BP (Fig. 4a). After 3.3 ka BP the sediment shows a fining trend, visible in e.g. the $\overline{SS}$ -values and EM1 abundance.

The late Holocene (<2.2 ka BP) is characterized by a further fining. Sand-sized material is nearly absent, GSDs are polymodal, normally distributed and show a poor sorting. The grain size of the coarse mode decreases slightly, while the fine mode remains stable. EM2 is only sparsely observed in this interval and EM1 dominates the siliciclastic sediment fraction with an average contribution of around 88 vol%. $\overline{SS}$ reaches overall minimum values of ~24 μm and a pronounced minimum of 21 μm at 0.4–0.8 ka BP.

### 3.3. Siliciclastic sediment elemental composition (XRF)

Al and Si display a continuous decrease throughout the core. In contrast, Fe and Ti show a slight increase, illustrating a gradual shift from Si & Al-pre-eminence in the Early Holocene to an Fe & Ti-dominance in the late Holocene. Prominent features are visible in all element records between ~8.4 and 8.0 ka BP and around 5.8 ka BP. Al and Si counts decrease sharply, while Ti and Fe counts increase sharply, often reaching overall highest or lowest values, respectively.

## 4. Discussion

### 4.1. Sediment-delivery processes

Located in a shelf trough that (i) interrupts the along-coast transport by the WGC and that (ii) connects the local, onshore sediment source with the open Labrador Sea, sedimentation at site GeoB19905-1 is likely affected by more than one sediment source and delivery process. Indeed, the two endmembers resulting from the grain-size analyses allow us to differentiate two major sediment transport pathways.

The polymodality and poor sorting of the fine EM1 indicate (a) a short transport distance not leaving enough time for hydrodynamic sorting and (b) the presence of different sediment constituents. This points to a rather proximal source providing glacially eroded material. Glacial erosion tends to produce polymodal sediments as a consequence of the different erosional processes and eroded rocks involved (e.g., crushing vs. abrasion) (Boulton, 1978; Haldorsen, 1981). In fact, the presence of such a polymodal fine EM

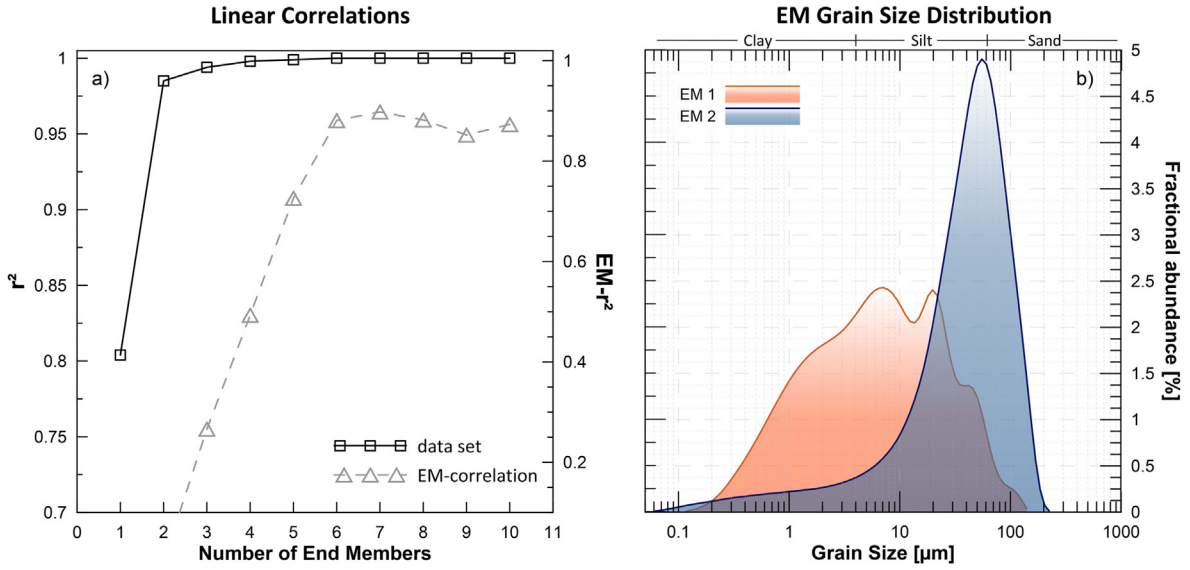


**Fig. 3.** a) Quality-of-Fit data for non-parametric end-member (EM) analysis on grain-size data of core GeoB19905-1. Solid black line and squares are the model misfit to the whole data set; the grey dashed line and triangles show the maximum squared linear correlation between the different fitted EMs as a measure of the linear independence of the EMs. [b]) Grain-size distribution of the two chosen EMs.

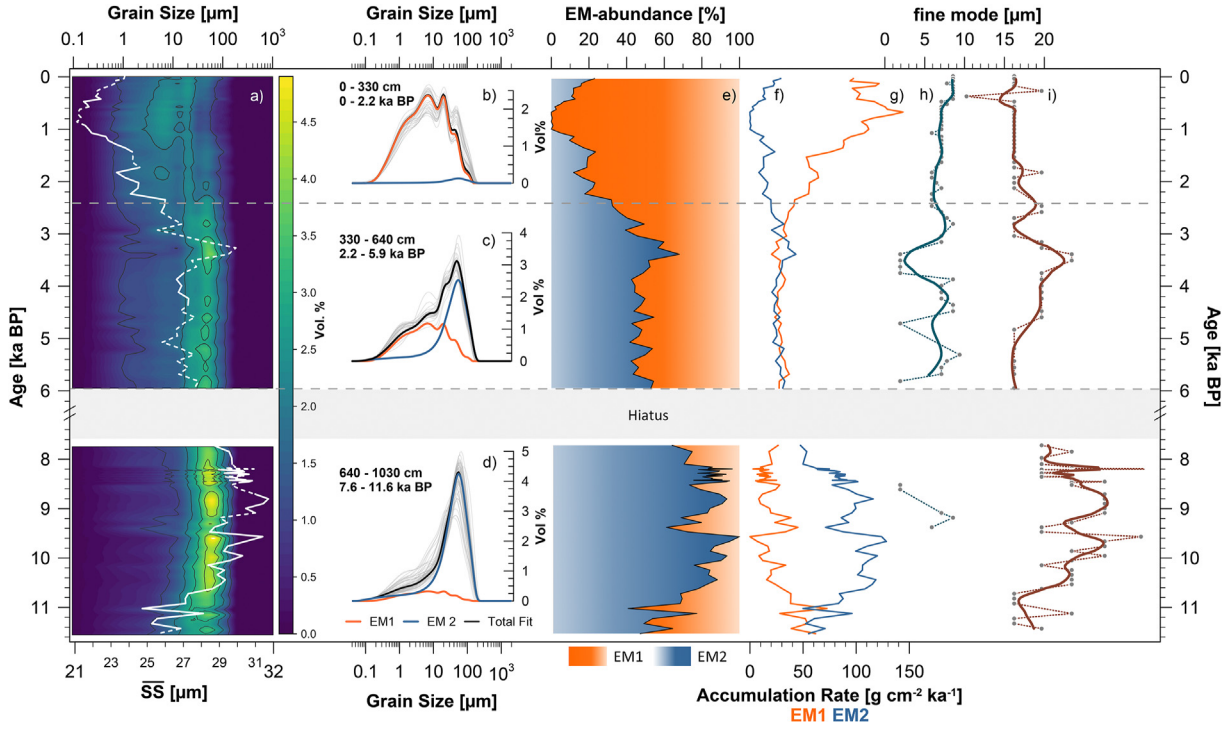


**Fig. 4.** Results of the grain-size analysis from core GeoB19905-1. A) shows a contour plot of the overall grain-size distribution overlain by the $\overline{SS}$ record (white line, stippling denotes less reliable (see section 4.1) intervals). Panels b, c, and d give size spectra of all individual samples (grey) in the respective intervals as well as abundances of the determined endmembers (EM1 in orange, EM2 in blue, EM total fit in black) for the samples at 130 cm, 440 cm and 850 cm core depth, respectively. E) gives the abundance of the two EMs, while f) and g) show their respective accumulation rates. h) and i) show the fine and coarse modal grain sizes, including a LOESS fit. (For interpretation of the references to colour in this figure legend, the reader is referred to the Web version of this article.)

has previously been recorded from the wider North Atlantic and interpreted to be the result of glacial erosion (Fillon and Full, 1984). Thus, the short transport route points to the nearby Greenland coast as the major source region, where lots of glacially eroded sediment is provided by the glaciers of the GrIS.

In principle, two transport pathways of the poorly sorted, glacial sediments of EM1 from the coast through the Sukkertop trough to the core site are possible: (i) within a buoyant surface plume derived from glacial meltwater that overlies the saltier marine water, or (ii) as near-bed transport similar to hyperpycnal currents. The volumetrically more important plume-transport (>75% in SE Greenland, Hasholt (1996)) entails seaward sediment transport in suspension, in places potentially enhanced by estuarine fjord circulation (Chu et al., 2012; Rasch et al., 2000), until reaching the

shelf. Here, the change in salinity and the turbulent mixing with the WGC can cause flocculation (Szczuciński and Zajączkowski, 2013) and create and maintain negative buoyancy (Wright, 2012), supporting the rapid settling of the material in the trough. We note, however, that high WGC-flow most likely prevents substantial deposition of EM1. Alternatively, the near-bed transport would be initiated if incoming meltwater carries such a high sediment load that its density exceeds the density of seawater (>43.49 kg m-3, for lat. >50°, Mulder and Syvitski (1995), or, if convective instability is considered, that its sediment load is at least 5 kg $m^{-3}$ (Parsons et al., 2001). This would result in its rapid descent already close to shore and transport along the seabed to the core site (Wright, 2012) by a hyperpycnal plume-like transport (see e.g. Mulder et al. (2003) for a review). This transport pathway would be much less affected by the fast-flowing WGC, as the sediment-laden flow dives under the core of the WGC. Both transport pathways can deliver the polymodal, fine EM1 sediments from a nearby onshore source to the core site and cannot be differentiated by the available data.

In contrast, the unimodal nature, the very good sorting, and the rather coarse grain size of EM 2 indicate transport and sorting by a strong current. The good sorting might imply either a rather long-range transport or a pre-sorted source material; a distinction between the two is not possible from the available grain-size data.

The strongest regional current, the northward flowing WGC, is the most probable carrier of EM2, delivering it from a southern source to the study site. Most likely, the WGC picks up glacial sediments from the shelf pre-sorted by earlier erosion/winnowing. As soon as the suspended sediment passes over the Sukkertop trough, the transport capacity of the WGC drops due to the sudden increase in water depth and the coarse material falls out of suspension. This hypothesis is supported by modelling studies (Klinck, 1996) and has been similarly described off Argentina (Voigt et al., 2013) and in the Gulf of Cadiz (Marchès et al., 2007). Thus, both quantity of EM2 through time and the dominant mode within the grain-size range of EM2-sediments are essentially controlled by the speed of the WGC (Fig. 4).

Varying contributions of EM1 and EM2 to sediment deposition in the Sukkertop trough, thus, represent two independent hydrodynamic regimes, with independent transport mechanisms from two different sources. While EM2 primarily depends on the strength of the WGC, EM1 is predominantly controlled by glacial erosion and meltwater supply to the sea, but might additionally be affected by the WGC preventing its deposition in the Sukkertop trough (only if transported by a buoyant surface plume). While the latter would imply a functional link between the deposition of the two end-members, the low correlation between their accumulation rates ($r^2 = 0.32$) suggests a largely independent deposition of EM1 and EM2 and might, in fact, favour an EM1 deposition by near-bed downslope sediment transport (see second transport pathway model above (cf. Wright et al., 2002)). Time averaging per sample is, on average, 11 years; the co-occurrence of both end-members within one sample shows that both processes can be contemporaneously active on these timescales, although we note that this could entirely be caused by bioturbation. The co-occurrence of both endmembers within nearly the entire core record implies that both processes were more or less contemporaneously active throughout the entire Holocene.

This understanding of the depositional regime is crucial for the correct interpretation of our $\overline{SS}$ data. While the reliability of $\overline{SS}$ in glaciated environments has been questioned in the past (Jonkers et al., 2015; Wu et al., 2018), McCave and Andrews (2019b) showed that $\overline{SS}$ does produce reliable current vigour estimates in glaciated environments, as long as it is current-transported prior to deposition. However, our grain-size data and the EM analysis show that this current transport is not necessarily always given in the present case. The deposition of EM1 is significantly influenced by the amount of glacially eroded material that is produced onshore and its polymodal distribution suggests no or only minor current-sorting prior to deposition. As the majority of our record, however, is dominated by the well-sorted, current-controlled EM2 having a dominant mode in the sortable silt range, we consider the $\overline{SS}$ record reliable for this period. Applying the reliability-check for $\overline{SS}$ (running downcore correlation between %SS and $\overline{SS}$, McCave and Andrews (2019b)), we find that, even for periods of dominant input of EM1, the correlation between %SS and $\overline{SS}$ is mostly >0.5, implying a reliable current speed reconstruction. Still, we note that $\overline{SS}$ might overestimate the reduction in current speed in the upper part of the core where an increased input of the non-current sorted EM1 is evident. Periods of suspect $\overline{SS}$ are also recorded over parts of the mid-Holocene, e.g. just after the hiatus and around 3.5 ka BP (see Fig. 3). We aim to overcome this by also using the fine and coarse modes. The coarse mode falls (almost exclusively) into the grain size spectrum of the current controlled EM2, while the fine mode is most likely representing the modal grain size of the fine, locally sourced EM1.

### 4.2. AW-inflow to the Labrador Sea during the Holocene

As outlined above, the history of the inflow of AW via the WGC to our study area in the eastern Labrador Sea can be inferred from a combination of the $\overline{SS}$ record, the sediments coarse mode and the input and accumulation of the current-controlled EM2 obtained from the siliciclastic sediment faction at our core site in the Sukkertop trough. The results reveal a characteristic pattern marked by moderate flow speeds in the earliest Holocene preceding a rise to maximum current speeds in the early Holocene, which is followed by a gradual decrease towards modern times and a pronounced minimum in the last ~2 ka BP.

During the earliest Holocene, moderate flow speeds are recorded from 11.6 to 10.6 ka BP, suggesting a moderate AW-inflow via the WGC. This interpretation is in line with other records of perturbations of the North Atlantic circulation during the late Deglacial as an effect of the sustained meltwater input (Hoffman et al., 2012; Hoogakker et al., 2011; Ólafsdóttir et al., 2010; Thornalley et al., 2013). In this case, especially the synchronous deglaciation of the Laurentide Ice Sheet (LIS) (Andrews et al., 1999; Carlson et al., 2008) and SW-GrIS (Briner et al., 2016; Larsen et al., 2014; Weidick et al., 2012; Young and Briner, 2015) in the earliest Holocene functioned as potential meltwater sources.

The $\overline{SS}$ records obtained upstream of our core site in the eastern Labrador Sea, e.g. MD99-2269 north of Iceland and JM96-1206 off SE Greenland (McCave and Andrews, 2019a), indicate fastest flow of the respective waters within the time window 9.7 to 7.2 ka BP, roughly in line with the highest current speeds indicated at our core site (Fig. 6). McCave and Andrews (2019a) termed this phenomenon the Holocene Speed Maximum (HSM), which we now document in the Labrador Sea for the first time. However, the regional HSM in the Labrador Sea already began at 10.6 ka BP and, thus, approximately 1 ka earlier than at sites off East Greenland (JM96-1206) and North Iceland (MD99-2269). This early HSM onset likely has its roots in an increased vigour in the southern branch of the Irminger Current-component of the WGC (cf. Praetorius et al. (2008), see Fig. 1), which is admixed downstream of the East Greenland and North Iceland sites and hence does not influence current speeds there. Adding our observations to the HSM data of McCave and Andrews (2019a) and additionally considering the ISOW-stack (Thornalley et al., 2013) as well as the AMOC-record of

Ritz et al. (2013), both also showing an onset around 10.8 and 10.6 ka BP, the time frame of the HSM as a whole might need to be extended to 10.6–6 ka BP. Thus, the HSM reported at these sites most likely represents the full re-establishment of the North Atlantic circulation after the Deglacial slow-down.

For the mid-Holocene after the hiatus, our record indicates a slowdown of AW inflow that levels to pre HSM-speeds, again mirroring the North Atlantic-wide trend (McCave and Andrews, 2019a; Thornalley et al., 2013) in agreement with a slowdown of the AMOC (Ritz et al., 2013). This decreasing AW-inflow to the eastern Labrador Sea is also reflected by decreasing sea-surface salinities in the southern Labrador Sea (Solignac et al., 2004). In contrast, several studies from the area suggest an increased inflow of AW at this time (De Vernal et al., 2013; Saini et al., 2020; Seidenkrantz et al., 2013) largely based on surface water proxies. This is even thought to have initiated or at least fostered deep-water formation in the Labrador Sea (cf. Hillaire-Marcel et al., 2001) starting around 7 ka BP. While we do not question the possibility of a major (surface) hydrographic change around 7 ka BP, our grain-size data clearly show that the vigour of AW-inflow was decreasing at that time - in line with reduced current speeds in the North Atlantic (McCave and Andrews, 2019a; Thornalley et al., 2013). The apparent contradiction paradox between these datasets might be explained by the stratifying effects of a meltwater lens (see section 4.3).

During the mid/late Holocene transition, the significant fining of the $\overline{SS}$, accompanied by a contemporaneous fining of the coarse mode and a slight decrease of EM2-AR between 3.3 and 2 ka clearly suggests a further slowdown of the WGC off SW Greenland. As this slowdown coincides with the onset of the Neoglaciation, i.e. the period defined by the cooling following the Holocene Thermal Maximum (Briner et al., 2016; Jennings et al., 2002; Reusche et al., 2014; Weidick et al., 2012), this phenomenon is now termed the Neoglacial Slowdown of the WGC.

The significant increase in input of the locally-derived EM1 during the latest Holocene (<1.5 ka) is interpreted to reflect the neoglacial GrIS advances and related increased sediment delivery to the shelf. This means that the contemporaneous drop in the $\overline{SS}$ likely overestimates the current-speed reduction due to a larger influence of the non-current-sorted EM1 on $\overline{SS}$.

### 4.3. The Holocene AW paradox: inflow vs. influence

While there is ample evidence for warming and salination of the surface waters in the eastern Labrador Sea and Baffin Bay after ~7 ka BP that is often referred to enhanced *AW-inflow* via the WGC (Gibb et al., 2015; Moros et al., 2016), our record, in line with the larger North Atlantic current regime (McCave and Andrews, 2019a; Thornalley et al., 2013), clearly shows a considerable simultaneous decrease in WGC-speed. This apparent Holocene AW paradox can be reconciled by the (often lacking) distinction between *AW-inflow* and AW-*influence*.

Stronger WGC-inflow to the Labrador Sea and Baffin Bay starting ~7 ka BP has been inferred from proxy-based indications for rising sea-surface temperatures (SSTs) and salinities (SSSs) (Ouellet-Bernier et al., 2014), decreasing sea ice cover (e.g. Saini et al., 2020), the initiation of deep convection in the Labrador Sea (cf. Hillaire-Marcel et al., 2001), or bottom-water warming (Hansen et al., 2020; Moros et al., 2016), while others point to a stronger influence of the AW to explain the observed changes (Caron et al., 2019; Gibb et al., 2014). In this context, it is important to point out that the inferred increase in inflow is in contrast to our direct reconstructions of the WGC strength pointing to a decrease in WGC inflow at this time. However, this does not exclude the possibility for an increased AW-influence transported via the WGC.

This paradox can be explained by considering another major environmental change affecting the north western North Atlantic between 8 and 7 ka BP: the cessation of large-scale GrIS/LIS melting (Fairbanks, 1989; Funder et al., 2011; Peltier and Fairbanks, 2006) and, accordingly, the strong reduction or even disappearance of a pronounced meltwater lens in the Labrador Sea (Hillaire-Marcel et al., 2001; Seidenkrantz, 2013). In the early Holocene, fast ice sheet retreat and associated melting caused a large freshwater input into the Labrador Sea and Baffin Bay, effectively capping the underlying warmer waters of the WGC. As the strong meltwater input waned after ~7 ka BP (Fairbanks, 1989; Funder et al., 2011; Peltier and Fairbanks, 2006), a strongly reduced meltwater lens allowed for a shoaling of the WGC, explaining why it could exert a stronger influence on the surface waters. As a result, especially the plankton-based surface water proxies reflect warming, salination and decreasing sea ice cover (Caron et al., 2019; Gibb et al., 2015; Saini et al., 2020). Along the same line of thought, the decreasing sea ice cover might have triggered enhanced productivity, explaining the observed changes in the benthic foraminifera community within the depth reach of the WGC in the eastern Baffin Bay that previously have been related to bottom-water warming (Moros et al., 2016; Perner et al., 2013). Consequently, these changes can be interpreted to reflect a stronger WGC influence as also entertained by earlier studies (e.g. Caron et al., 2019; Gibb et al., 2014), despite actually decreasing WGC inflow. This would also explain the initiation of deep convection in the Labrador Sea around that time (Hillaire-Marcel et al., 2001), as deep convection relies on an efficient heat exchange between the ocean and atmosphere – a scenario that is incompatible with the presence of a sustained meltwater lens.

The controlling role of a prominent meltwater lens in the Labrador Sea and Baffin Bay in the early Holocene could also explain the partial mismatch between the time-transgressive regional onsets of the Holocene Thermal Maxima (HTM), ranging from 9 to 5 ka BP around Denmark Strait to 6 to 4 ka BP in SW Greenland (Kaufman et al., 2004). While the general importance of oceanic heat transport in the North Atlantic is highlighted in several studies (Hoffmann et al., 2019; Myers et al., 2007; Thornalley et al., 2010), the onset of the HTM in SW-Greenland actually follows the end of the HSM (cf. McCave and Andrews (2019a), this study). Thus, the regional HTM in SW Greenland is most likely not triggered by enhanced oceanic heat transport, but by enhanced ocean-atmosphere heat exchange enabled by the reduction of the insulating meltwater lens.

### 4.4. The enigmatic signature of short- and long-term ice sheet-ocean interaction

Once the reduced meltwater lens allowed for enhanced ocean-atmosphere heat exchange, variations in oceanic heat transport due to variations in WGC inflow could affect the regional setting. The late Holocene slowdown of the WGC after 3 ka BP coincides with the onset of the regional Neoglaciation as evident in several onshore (D'Andrea et al., 2011; Schweinsberg et al., 2017) and offshore (Andrews et al, 2010, 2016; Li et al., 2017) records and in reconstructions of the size of the GrIS (Larsen et al., 2015; Lecavalier et al., 2014) (Fig. 7). Thus, it is suggested that decreasing oceanic heat transport by the WGC in the late Holocene – in line with the further decreasing insolation – contributed to the Neoglaciation in Greenland. As the current speed continued to wane and the Neoglaciation progressed, the ice margin advanced towards the coast, delivering more and more fine, glacially eroded sediment to the shelf. Accordingly, we record the strong increase in EM1 only in the latest Holocene, i.e. approximately 1.5 ka after the onset of the

Neoglaciation. Here, a positive feedback loop with the local meltwater plumes transporting the EM1-sediments might have helped to sustain the neoglacial cooling trend (cf. e.g. Gajewski (2015). In this scenario, a mechanism similar to the early Holocene, where a meltwater lens capped off the warmer WGC waters, would be active. Both mechanisms effectively reduce heat flux from the ocean to the atmosphere, explaining the progressing cooling. This notion is supported by data from the nearby Ameralik fjord, from which contemporaneously enhanced sea-ice cover and increased water-column stratification were reported (Møller et al., 2006), and from the western Labrador Sea, where the reported surface-water cooling similarly preceded an increased presence of sea-ice and/or meltwater (Lochte et al., 2019). In addition to an enhanced stratification, Møller et al. (2006) also suggested a synchronous decrease in meltwater-derived sediment input into Ameralik fjord, which is in contrast to the enhanced deposition of finer material observed at site GeoB19905. This offset probably results from the very different sedimentary settings within the fjord compared to the outer shelf setting studied here. The confined conditions within a fjord setting result in a more locally controlled sedimentation, while the spatially larger influences on the sedimentation on the shelf also invoke different sediment sources (i.e., local vs. regional) and pathways.

While the grain-size data provide information on the sedimentation processes, the XRF data document the geochemical composition of the sediments and can thus provide additional information on the sediment source region. The increasing EM1 input during the Neoglaciation is accompanied by a change in the elemental composition of the sediments marked by increasing Fe/Si and Ti/Al ratios (Fig. 5). Indeed, also the long-term increase in the element ratios throughout the entire Holocene is consistent with the continuously increasing admixture of EM1 sediments that are interpreted to reflect a local sediment source. Thus, the locally sourced EM1 material delivered to the core site during the Neoglaciation appears to be geochemically characterized by relatively high Fe and Ti and low Si and Al contents, while in contrast EM2,

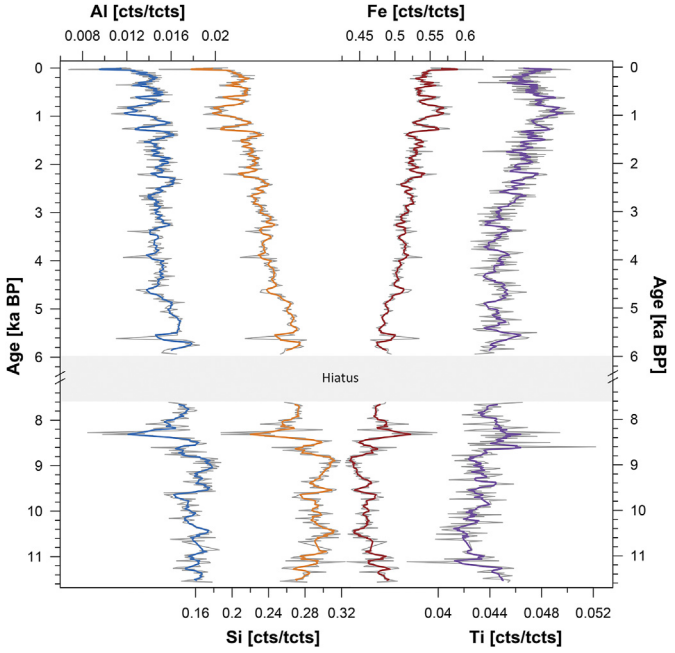


**Fig. 5.** XRF-counts of major elements measured on core GeoB19905-1 illustrating 1) the gradual shift from a Si & Al-pre-eminence in the early Holocene to a Fe & Ti-dominance in the late Holocene and 2) the pronounced excursions in all elemental records around 8.2 and 5.8 ka BP.

dominant prior to the Neoglaciation, appears to be associated with higher Si and Al contents. Exploration studies from the Sinarsuk deposit in vicinity to the core site showed significant amounts of ilmenite and magnetite in the host rock, thereby potentially providing a source for the elevated Fe and Ti- contents (Grammatikopoulos et al., 2002; Secher, 1980). Additional support for this interpretation is provided by Bhatia et al. (2013) who documented elevated dissolved and particulate Fe concentrations in meltwater plumes off West Greenland and Leng et al. (2018) who showed increased hematite and magnetite contents in plumite deposits off eastern Canada.

In addition to this long-term trend, the most prominent features in the XRF data are peaks in the Fe/Si and Ti/Al ratios at around 8.2 and 5.8 ka BP (Fig. 7). Interestingly, despite their distinct expression in the XRF record, these peaks are not associated with any changes in the EM2-dominated grain-size distribution prevailing around these events. Consequently, this observation points to the short-term deposition of comparably coarse, yet locally-sourced Fe- and Ti-rich material to the core site. To explain such a scenario, the nature of these events has to be considered.

The "8.2 ka – event" is a globally well-documented cooling episode that was most probably caused by the injection of large volumes of meltwater into the Labrador Sea as part the final collapse of the LIS, when the glacial lakes Ojibway and Agassiz suddenly drained into the ocean. This led to a reduced strength of the subpolar gyre circulation, disrupting heat and energy transport, in turn causing temperature drops in the order of 5–7 °C (Alley et al., 1997; Alley and Ágústsdóttir, 2005). This cooling has been linked to records of glacial advances in southern and central Greenland (Balascio et al., 2015; Schweinsberg et al., 2017) (Fig. 7). The 5.8 ka-event appears to be similar in its expression, but smaller in magnitude as well as spatial reach, as it is currently only reported from the western Greenland margin (Fig. 7), while it is not (yet) documented in SE-Greenland (cf. Balascio et al., 2015; Schweinsberg et al., 2017).

Having previously established that the high sedimentary Fe and Ti signatures in the Neoglaciation result from additional sediment input caused by local glacial advances, we can infer that the high Fe and Ti signatures during the 8.2 and 5.8 events also represent local glacier advances. In contrast to the Neoglaciation, however, the WGC current speeds remained high during these events as indicated by the EM2 dominance. This explains why, despite the activation of the local source, only coarse Fe- and Ti-rich material was transported to the core site, while all finer material was winnowed away. Such effective winnowing implies that most of the input and transport of sediment must have occurred via the "plume model" outlined in section 4.1. Thus, the local expression of the 8.2 ka and 5.8 ka-events in the north eastern Labrador Sea is merely given by enhanced input of locally-derived material reflecting glacier advances related to these events and not by hydrodynamic perturbations. As these events had therefore no impact on the AW-inflow via the WGC, our findings in turn document that on such short timescales and/or under the presence of a sustained meltwater lens (see section 4.3), ice sheet dynamics and AW-inflow did not influence each other.

Interestingly, another well-documented cooling event at 9.2 ka BP (Fleitmann et al., 2008) left no geochemical signature in the sediments of core GeoB19905-1 but might correspond to a short-lived decrease in current speed at 9.2 ka BP. According to Fleitmann et al. (2008), the 9.2 ka-event was caused by a meltwater outburst much smaller than that during the 8.2 ka-event but similar in mechanism. A possible explanation for the dissimilar expressions of these events lies in their different meltwater routings (Fleitmann et al., 2008; Teller and Leverington, 2004). During the 9.2 ka-event, the still relatively stable and extended LIS blocked

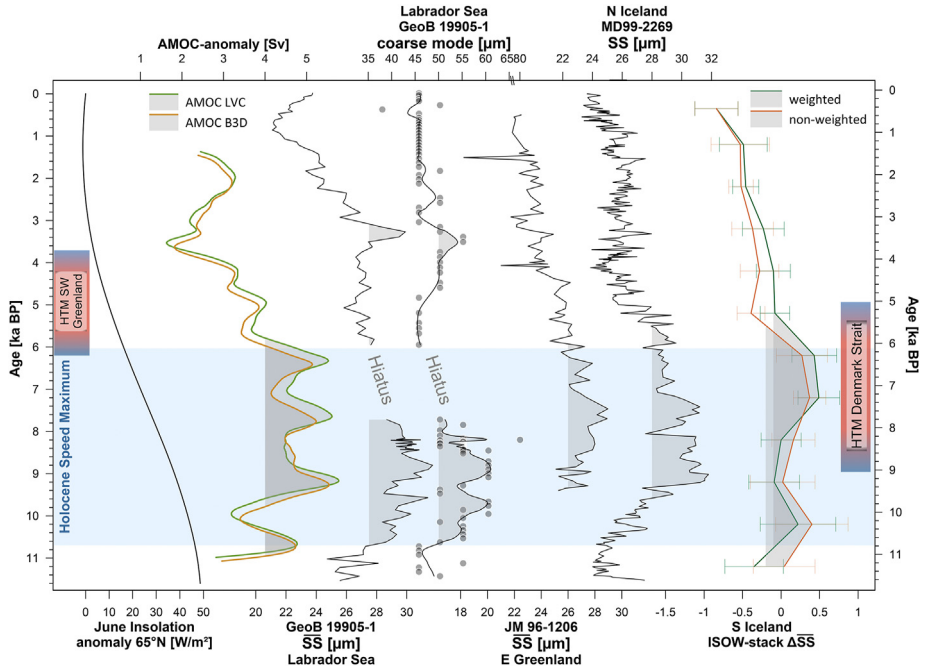


**Fig. 6.** Compilation of current strength reconstructions from the North Atlantic in relation to insolation and regionally varying Holocene Thermal Maxima (after (Kaufman et al., 2004)), grey shaded areas mark the respective Holocene Speed Maxima, blue shading indicates general HSM-timeframe. AMOC anomaly from Ritz et al. (2013), JM96-1206 and MD99-2269 sortable silt mean grain size ($\overline{SS}$) from McCave and Andrews (2019a), Iceland-Scotland Ridge Overflow Water (ISOW)-stack from Thornalley et al. (2013). (For interpretation of the references to colour in this figure legend, the reader is referred to the Web version of this article.)

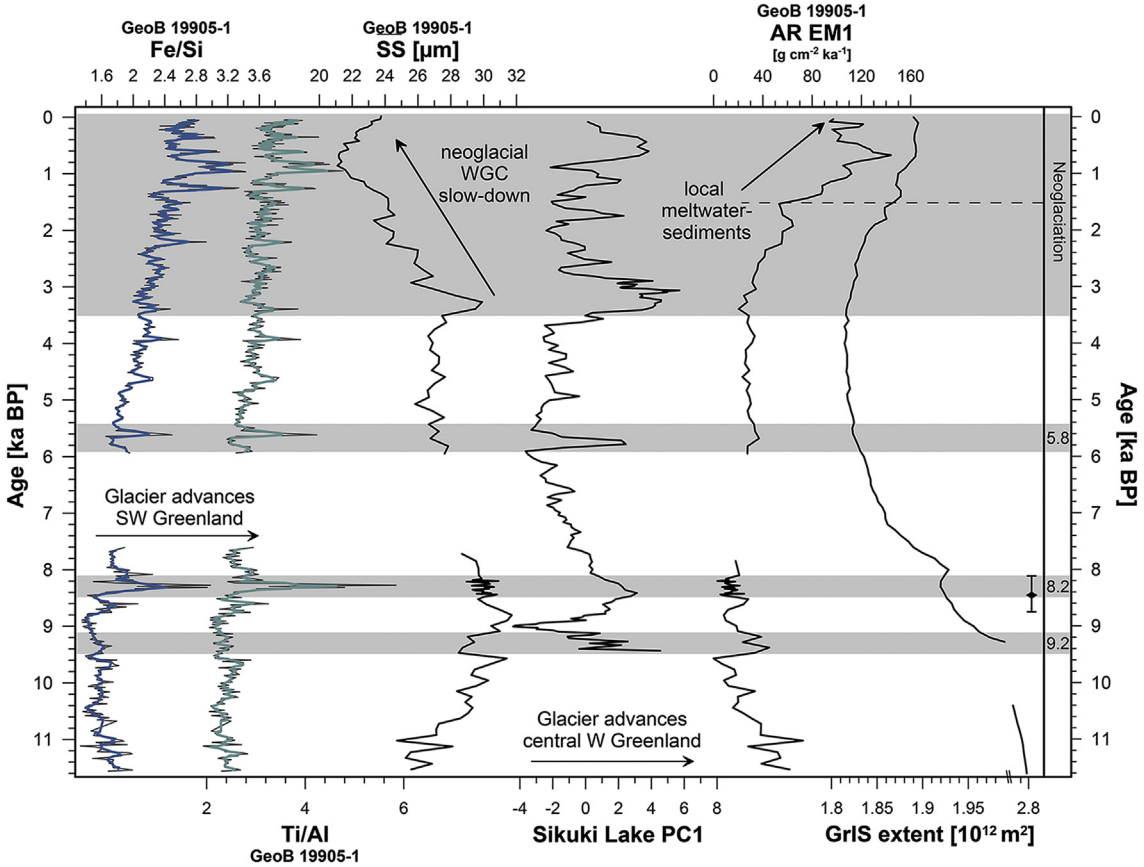


**Fig. 7.** Elemental records of on-and offshore sediment cores (GeoB19905-1 (this study) and Sikuki Lake (Schweinsberg et al., 2017) indicative of glacier advances alongside WGC current speed data, and accumulation rates of end member 1 next to modelled GrIS-extent (Lecavalier et al., 2014). Grey bars mark short-term excursions in either the XRF or grain size data at 9.2, 8.2 and 5.8 ka BP as well as the longer trends during the Neoglaciation, error bar indicates duration of terminal outbursts of Lake Agassiz and Ojibway (after Barber et al. (1999).

the northerly drainage route via the Hudson Bay and most of the meltwater entered the southern Labrador Sea via the St. Lawrence estuary, whereas the majority of the final drainage of Lake Agassiz around 8.2 ka BP is thought to have occurred further north via Hudson Bay (Fleitmann et al., 2008; Hillaire-Marcel et al., 2007; Teller and Leverington, 2004). The more southerly injection of meltwater during the 9.2 ka BP-pulse meant that it exerted a more direct influence on the hydrography of the north-western North Atlantic and was therefore probably able to locally slow down the WGC, despite the lower volume of injected meltwater and without causing noticeable glacier advances in SW Greenland.

## 5. Conclusion

The combined high-resolution records of grain-size changes and elemental composition presented in this study reveal long- and short-term variability in sediment transport, deposition and source area activity affecting our core site off SW Greenland during the last 11.6 ka BP. The record is marked by a gradual shift from a dominantly current-/pre-sorted sediment in the early and mid-Holocene towards a prevalent input of a locally sourced, poorly sorted sediment. Given the mainly current controlled sedimentation, we are able to present a robust and direct record of WGC-speeds and according AW-inflow to the Labrador Sea throughout the Holocene.

Highest WGC current speeds are recorded in the early Holocene (>7.6ka BP), confirming the presence of the HSM also for the Labrador Sea. A gradual decrease towards the mid-Holocene is followed by lowest WGC speeds after 3 ka BP. This temporal pattern of our current-speed record is in excellent agreement to comparable records within the North Atlantic indicating that the current regime in the Labrador Sea is closely coupled to the overall current regime of the North Atlantic, highlighting that the surface and intermediate circulation in the Labrador Sea have been a vital part of the AMOC in the Holocene.

Our current speed data shed new light on an important aspect of palaeoceanographic studies in the Labrador Sea and Baffin Bay: the need for a careful differentiation between AW-inflow via the WGC and AW-influence on surface waters as well as a careful consideration of the actual vertical water-mass structure. Our record shows that AW-inflow via the WGC has been decreasing, when surface water warming and salination are reported from many other sites in the Labrador Sea and Baffin Bay around 7.5 ka BP. We are able to explain this paradox by considering the insulation effect of a meltwater lens that prevailed until ~7.5 ka BP. As the meltwater input waned, the WGC could shoal, allowing warming and salination of surface waters as well as an efficient heat exchange with the atmosphere.

Combining grain-size data with elemental records, we are able to show that during the Neoglaciation as well as during short-term events at 8.2 and 5.8 ka BP geochemically distinct material from a local source was deposited in the Sukkertop trough. Given the synchronicity with widespread and local environmental perturbations (especially around 8.2 ka BP), this additional input is most likely related to glacier advances in SW Greenland as a consequence of short-term atmospheric cooling. Interestingly, these events are not marked by perturbation in the WGC speed. In contrast, a short-term slow-down of the WGC that is not reflected in sediment geochemistry is recorded around 9.2 ka BP, potentially presenting the local expression of the 9.2 ka event (cf. Fleitmann et al., 2008) in the north-eastern Labrador Sea.

## Author statement

Jens Weiser: Investigation, Formal analysis, Data curation, Methodology, Visualization, Writing – original draft, Writing – review & editing, Jürgen Titschack: Resources, Data curation, Writing – review & editing, Supervision. Markus Kienast: Writing – review & editing, Supervision. Ian Nicholas McCave: Methodology, Data curation, Writing – review & editing. Annalena Antona Lochte: Writing – review & editing. Jeetendra Saini: Data curation, Writing – review & editing, Rüdiger Stein: Data curation, Writing – review & editing, Supervision. Dierk Hebbeln: Conceptualization, Investigation, Writing – review & editing, Supervision, Funding acquisition, Project administration.

## Declaration of competing interest

The authors declare that they have no known competing financial interests or personal relationships that could have appeared to influence the work reported in this paper.

## Acknowledgements

The master and crew of the R/V Maria S. Merian are gratefully acknowledged for support of the work during cruise MSM44. This project was supported by the Deutsche Forschungsgemeinschaft (DFG) through the International Research Training Group “Processes and impacts of climate change in the North Atlantic Ocean and the Canadian Arctic” (IRTG 1904 ArcTrain). The authors are indebted to editor A. Voelker and the two anonymous reviewers for their invaluable comments.

## Appendix A. Supplementary data

Supplementary data to this article can be found online at https://doi.org/10.1016/j.quascirev.2021.106833.

## Data availability

Data related to this article are made available through PANGEA at https://www.pangaea.de/.

## References

Alley, R.B., Ágústsdóttir, A.M., 2005. The 8k event: cause and consequences of a major Holocene abrupt climate change. Quat. Sci. Rev. 24, 1123–1149. https://doi.org/10.1016/j.quascirev.2004.12.004.

Alley, R.B., Mayewski, P.A., Sowers, T., Stuiver, M., Taylor, K.C., Clark, P.U., 1997. Holocene climatic instability: a prominent, widespread event 8200 yr ago. Geology 25 (483). https://doi.org/10.1130/0091-7613(1997)025<0483:HCIAPW>2.3.CO;2.

Andrews, J.T., Jennings, A.E., Coleman, G.C., Eberl, D.D., 2010. Holocene variations in mineral and grain-size composition along the East Greenland glaciated margin (ca 67°-70°N): local versus long-distance sediment transport. Quat. Sci. Rev. 29, 2619–2632. https://doi.org/10.1016/j.quascirev.2010.06.001.

Andrews, J.T., Keigwin, L., Hall, F., Jennings, A.E., 1999. Abrupt deglaciation events and Holocene palaeoceanography from high-resolution cores, cartwright saddle, labrador shelf, Canada. J. Quat. Sci. 14, 383–397. https://doi.org/10.1002/(SICI)1099-1417(199908)14:5<383::AID-JQS464>3.0.CO;2-J.

Andrews, J.T., Stein, R.R., Moros, M., Perner, K., 2016. Late Quaternary changes in sediment composition on the NE Greenland margin (~73° N) with a focus on the fjords and shelf. Boreas 45, 381–397. https://doi.org/10.1111/bor.12169.

Bahr, A., Jiménez-Espejo, F.J., Kolasinac, N., Grunert, P., Hernández-Molina, F.J., Röhl, U., Voelker, A.H.L., Escutia, C., Stow, D.A.V., Hodell, D., Alvarez-Zarikian, C.A., 2014. Deciphering bottom current velocity and paleoclimate signals from contourite deposits in the Gulf of Cádiz during the last 140 kyr: an inorganic geochemical approach. Geochem. Geophys. Geosyst. 15, 3145–3160. https://doi.org/10.1002/2014GC005356.

Bakker, P., Van Meerbeeck, C.J., Renssen, H., 2012. Sensitivity of the north Atlantic climate to Greenland ice sheet melting during the last interglacial. Clim. Past 8, 995–1009. https://doi.org/10.5194/cp-8-995-2012.

Balascio, N.L., D'Andrea, W.J., Bradley, R.S., 2015. Glacier response to North Atlantic climate variability during the Holocene. Clim. Past 11, 1587–1598. https://doi.org/10.5194/cp-11-1587-2015.

Bamberg, A., Rosenthal, Y., Paul, A., Heslop, D., Mulitza, S., Rühlemann, C., Schulz, M., 2010. Reduced North Atlantic central water formation in response to early Holocene ice-sheet melting. Geophys. Res. Lett. 37, 1–5. https://doi.org/10.1029/2010GL043878.

Barber, D.C., Dyke, A.S., Hillaire-Marcel, C., Jennings, A.E., Andrews, J.T., Kerwin, M., Bilodeau, B., McNeely, R.N., Southon, J., Morehead, M.D., Gagnon, J.M., 1999. Forcing of the cold event of 8,200 years ago by catastrophic drainage of Laurentide lakes. Nature 400, 344–348. https://doi.org/10.1038/22504.

Batchelor, C.L., Dowdeswell, J.A., 2014. The physiography of high Arctic cross-shelf troughs. Quat. Sci. Rev. 92, 68–96. https://doi.org/10.1016/j.quascirev.2013.05.025.

Batchelor, C.L., Dowdeswell, J.A., Rignot, E., 2018. Submarine landforms reveal varying rates and styles of deglaciation in north-west Greenland fjords. Mar. Geol. 402, 60–80. https://doi.org/10.1016/j.margeo.2017.08.003.

Bhatia, M.P., Kujawinski, E.B., Das, S.B., Breier, C.F., Henderson, P.B., Charette, M.A., 2013. Greenland meltwater as a significant and potentially bioavailable source of iron to the ocean. Nat. Geosci. 6, 274–278. https://doi.org/10.1038/ngeo1746.

Blaauw, M., Christen, J.A., 2018. Rbacon: age-depth modelling using bayesian statistics. R package version 2.3.4, pp. 1–14. https://CRAN.R-project.org/package=rbacon.

Blaauw, M., Christen, J.A., 2011. Flexible paleoclimate age-depth models using an autoregressive gamma process. Bayesian Anal 6, 457–474. https://doi.org/10.1214/11-BA618.

Blott, S.J., Pye, K., 2001. GRADISTAT: a grain size distribution and statistics package for the analysis of unconsolidated sediments. Earth Surf. Process. Landforms 26, 1237–1248. https://doi.org/10.1002/esp.261.

Böning, C.W., Behrens, E., Biastoch, A., Getzlaff, K., Bamber, J.L., 2016. Emerging impact of Greenland meltwater on deepwater formation in the North Atlantic Ocean. Nat. Geosci. 9, 523–527. https://doi.org/10.1038/ngeo2740.

Boulton, G.S., 1978. Boulder shapes and grain-size distributions of debris as indicators of transport paths through a glacier and till genesis. Sedimentology 25, 773–799.

Boxberg, F., Asendorf, S., Bartholomä, A., Schnetger, B., de Lange, W.P., Hebbeln, D., 2020. Historical anthropogenic heavy metal input to the south-eastern North Sea. Geo Mar. Lett. 40, 135–148. https://doi.org/10.1007/s00367-019-00592-0.

Briner, J.P., McKay, N.P., Axford, Y., Bennike, O., Bradley, R.S., de Vernal, A., Fisher, D., Francus, P., Fréchette, B., Gajewski, K., Jennings, A.E., Kaufman, D.S., Miller, G.H., Rouston, C., Wagner, B., 2016. Holocene climate change in Arctic Canada and Greenland. Quat. Sci. Rev. 147, 340–364. https://doi.org/10.1016/j.quascirev.2016.02.010.

Buch, E., 2002. Present Oceanographic Conditions in Greenland Waters, Danish Meteorological Institute Scientific Report. Division for Operational Oceanography, Danish Meteorological Institut.

Buckley, M.W., Marshall, J., 2016. Observations, inferences, and mechanisms of the Atlantic meridional overturning circulation: a review. Rev. Geophys. 54, 5–63. https://doi.org/10.1002/2015RG000493.

Butzin, M., Köhler, P., Lohmann, G., 2017. Marine radiocarbon reservoir age simulations for the past 50,000 years. Geophys. Res. Lett. https://doi.org/10.1002/2017GL074688.

Carlson, A.E., Legrande, A.N., Oppo, D.W., Came, R.E., Schmidt, G.A., Anslow, F.S., Licciardi, J.M., Obbink, E.A., 2008. Rapid early Holocene deglaciation of the Laurentide ice sheet. Nat. Geosci. 1, 620–624. https://doi.org/10.1038/ngeo285.

Caron, M., Rochon, A., Montero-Serrano, J., St-Onge, G., 2019. Evolution of sea-surface conditions on the northwestern Greenland margin during the Holocene. J. Quat. Sci. 1–12. https://doi.org/10.1002/jqs.3146.

Chen, W., Guillaume, M., 2012. HALS-based NMF with flexible constraints for hyperspectral unmixing. EURASIP J. Appl. Signal Process. https://doi.org/10.1186/1687-6180-2012-54.

Chu, V.W., Smith, L.C., Rennermalm, A.K., Forster, R.R., Box, J.E., 2012. Hydrologic controls on coastal suspended sediment plumes around the Greenland Ice Sheet. Cryosphere 6, 1–19. https://doi.org/10.5194/tc-6-1-2012.

Cuny, J., Rhines, P.B., Kwok, R., 2005. Davis Strait volume, freshwater and heat fluxes. Deep. Res. Part I Oceanogr. Res. Pap. 52, 519–542. https://doi.org/10.1016/j.dsr.2004.10.006.

D'Andrea, W.J., Huang, Y., Fritz, S.C., Anderson, N.J., 2011. Abrupt Holocene climate change as an important factor for human migration in West Greenland. Proc. Natl. Acad. Sci. Unit. States Am. 108, 9765–9769. https://doi.org/10.1073/pnas.1101708108.

De Vernal, A., Hillaire-Marcel, C., Rochon, A., Fréchette, B., Henry, M., Solignac, S., Bonnet, S., 2013. Dinocyst-based reconstructions of sea ice cover concentration during the Holocene in the Arctic Ocean, the northern North Atlantic Ocean and its adjacent seas. Quat. Sci. Rev. 79, 111–121. https://doi.org/10.1016/j.quascirev.2013.07.006.

Dickson, R., Lazier, J., Meincke, J., Rhines, P., Swift, J., 1996. Long-term coordinated changes in the convective activity of the North Atlantic. Prog. Oceanogr. 38, 241–295. https://doi.org/10.1016/S0079-6611(97)00002-5.

Dorschel, B., Afanasyeva, V., Bender, M., Dreutter, S., Eisermann, H., Gebhardt, A.C., Hansen, K., Hebbeln, D., Jackson, R., Jeltsch-Thömmes, A., Jensen, L., Kolling, H., Duc, C. Le, Lenz, K.-F., Lübben, B., Madaj, L., Martínez-Méndez, G., Meyer-Schack, B., Schade, T., Siccha, M., Slabon, P., Wangner, D.J., Méndez, G.M., Meyer-Schack, B., Schade, T., Siccha, M., Slabon, P., Wangner, D.J., Kölling, H., Duc, C. Le, Lenz, K.-F., Lübben, B., Madaj, L., Méndez, G.M., Meyer-Schack, B., Schade, T., Siccha, M., Slabon, P., Wangner, D.J., Kolling, H., Duc, C. Le, Lenz, K.-F., Lübben, B., Madaj, L., Méndez, G.M., Meyer-Schack, B., Schade, T., Siccha, M., Slabon, P., Wangner, D.J., Kölling, H., Duc, C. Le, Lenz, K.-F., Lübben, B., Madaj, L., Méndez, G.M., Meyer-Schack, B., Schade, T., Siccha, M., Slabon, P., Wangner, D.J., 2015. Past Greenland Ice Sheet Dynamics, Palaeoceanography and Plankton Ecology in the Northeast Baffin Bay Cruise No. MSM44 30. MARIA S. MERIAN-Berichte, Bremen.

Dowdeswell, J.A., Hogan, K.A., Ó Cofaigh, C., Fugelli, E.M.G.G., Evans, J.R., Noormets, R., 2014. Late Quaternary ice flow in a West Greenland fjord and cross-shelf trough system: submarine landforms from Rink Isbrae to Uummannaq shelf and slope. Quat. Sci. Rev. 92, 292–309. https://doi.org/10.1016/j.quascirev.2013.09.007.

Driesschaert, E., Fichefet, T., Goosse, H., Huybrechts, P., Janssens, I., Mouchet, A., Munhoven, G., Brovkin, V., Weber, S.L., 2007. Modeling the influence of Greenland ice sheet melting on the Atlantic meridional overturning circulation during the next millennia. Geophys. Res. Lett. 34, 1–5. https://doi.org/10.1029/2007GL029516.

Duplessy, J.C., Labeyrie, L., Arnold, M., Paterne, M., Duprat, J., van Weering, T.C.E., 1992. Changes in surface salinity of the North Atlantic Ocean during the last deglaciation. Nature 358, 485.

Ellison, C.R.W., 2006. Surface and deep ocean interactions during the cold climate event 8200 Years ago. Science 312, 1929–1932. https://doi.org/10.1126/science.1127213.

Fairbanks, R.G., 1989. A 17,000-year glacio-eustatic sea level record: influence of glacial melting rates on the Younger Dryas event and deep-ocean circulation. Nature 342, 637.

Fillon, R.H., Full, W.E., 1984. Grain-size variations in North Atlantic non-carbonate sediments and sources of terrigenous components. Mar. Geol. 59, 13–50. https://doi.org/10.1016/0025-3227(84)90087-2.

Fleitmann, D., Mudelsee, M., Burns, S.J., Bradley, R.S., Kramers, J., Matter, A., 2008. Evidence for a widespread climatic anomaly at around 9.2 ka before present. Paleoceanography 23, 1–6. https://doi.org/10.1029/2007PA001519.

Funder, S., Kjeldsen, K.K., Kjær, K.H., O Cofaigh, C., 2011. The Greenland ice sheet during the past 300,000 Years: a review. Dev. Quat. Sci. 15, 699–713. https://doi.org/10.1016/B978-0-444-53447-7.00050-7.

Gajewski, K., 2015. Quantitative reconstruction of Holocene temperatures across the Canadian Arctic and Greenland. Global Planet. Change 128, 14–23. https://doi.org/10.1016/j.gloplacha.2015.02.003.

Ganachaud, A., Wunsch, C., 2000. Improved estimates of global ocean circulation, heat transport and mixing from hydrographic data. Nature 408, 453–456.

GEBCO Compilation Group, 2020. GEBCO 2020 Grid.

German Aerospace Center (DLR), 2018. TanDEM-X - Digital Elevation Model (DEM) - Global, p. 90m.

Gibb, O.T., Hillaire-Marcel, C., de Vernal, A., 2014. Oceanographic regimes in the northwest Labrador Sea since Marine Isotope Stage 3 based on dinocyst and stable isotope proxy records. Quat. Sci. Rev. 92, 269–279. https://doi.org/10.1016/j.quascirev.2013.12.010.

Gibb, O.T., Steinhauer, S., Frechette, B., de Vernal, A., Hillaire-Marcel, C., 2015. Diachronous evolution of sea surface conditions in the Labrador Sea and Baffin Bay since the last deglaciation. Holocene 25, 1882–1897. https://doi.org/10.1177/0959683615591352.

Grammatikopoulos, T., McKen, A., Hamilton, C., Christiansen, O., 2002. Vanadium-bearing magnetite and ilmenite mineralization and beneficiation from the Sinarsuk V-Ti project, West Greenland. Cim. Bull. 95, 87–95.

Haldorsen, S., 1981. Grain-size distribution of subglacial till and its realtion to glacial scrushing and abrasion. Boreas 10, 91–105.

Hansen, K.E., Giraudeau, J., Wacker, L., Pearce, C., Seidenkrantz, M.-S., 2020. Reconstruction of Holocene oceanographic conditions in the northeastern Baffin Bay. Clim. Past Discuss 1–34. https://doi.org/10.5194/cp-2019-152.

Hasholt, B., 1996. Sediment Transport in Greenland. Eros. Sediment Yield Glob. Reg. Perspect. IAHS Publi, pp. 105–114.

Heaton, T.J., Köhler, P., Butzin, M., Bard, E., Reimer, R.W., Austin, W.E.N., Bronk Ramsey, C., Grootes, P.M., Hughen, K.A., Kromer, B., Reimer, P.J., Adkins, J.F., Burke, A., Cook, M.S., Olsen, J., Skinner, L.C., 2020. Marine 20 - the marine radiocarbon age calibration curve (0-55,000 cal BP). Radiocarbon 62, 779–820. https://doi.org/10.1017/RDC.2020.68.

Hebbeln, D., Dokken, T., Andersen, E.S., Hald, M., Elverhøi, A., 1994. Moisture supply for northern ice-sheet growth during the Last Glacial Maximum. Nature 370, 357–360. https://doi.org/10.1038/370357a0.

Hebbeln, D., Henrich, R., Baumann, K.-H., 1998. Paleoceanography of the last interglacial/glacial cycle in the Polar North Atlantic. Quat. Sci. Rev. 17, 125–153. https://doi.org/10.1016/S0277-3791(97)00067-X.

Hillaire-Marcel, C., de Vernal, A., Bilodeau, G., Weaver, A.J.J.J., 2001. Absence of deep-water formation in the Labrador Sea during the last interglacial period. Nature 410, 1073–1077. https://doi.org/10.1038/35074059.

Hillaire-Marcel, C., de Vernal, A., Piper, D.J.W., 2007. Lake Agassiz final drainage event in the northwest North Atlantic. Geophys. Res. Lett. 34, 1–5. https://doi.org/10.1029/2007GL030396.

Hoffman, J.S., Carlson, A.E., Winsor, K., Klinkhammer, G.P., LeGrande, A.N., Andrews, J.T., Strasser, J.C., 2012. Linking the 8.2 ka event and its freshwater forcing in the Labrador Sea. Geophys. Res. Lett. 39, 2005–2009. https://doi.org/10.1029/2012GL053047.

Hoffmann, S.S., Dalsing, R.E., Murphy, S.C., 2019. Sortable silt records of intermediate-depth circulation and sedimentation in the southwest Labrador Sea since the last glacial maximum. Quat. Sci. Rev. 206, 99–110. https://doi.org/10.1016/j.quascirev.2018.12.028.

Hoogakker, B.A.A., Chapman, M.R., McCave, I.N., Hillaire-Marcel, C., Ellison, C.R.W., Hall, I.R., Telford, R.J., 2011. Dynamics of North Atlantic deep water masses during the Holocene. Paleoceanography 26, 1–10. https://doi.org/10.1029/2011PA002155.

Jackson, R., Carlson, A.E., Hillaire-Marcel, C., Wacker, L., Vogt, C., Kucera, M., 2017. Asynchronous instability of the North American-Arctic and Greenland ice

sheets during the last deglaciation. Quat. Sci. Rev. 164, 140–153. https://doi.org/10.1016/j.quascirev.2017.03.020.
Jakobsson, M., Mayer, L.A., Bringensparr, C., Castro, C.F., Mohammad, R., Johnson, P., Ketter, T., Accettella, D., Amblas, D., An, L., Arndt, J.E., Canals, M., Casamor, J.L., Chauché, N., Coakley, B., Danielson, S., Demarte, M., Dickson, M.L., Dorschel, B., Dowdeswell, J.A., Dreutter, S., Fremand, A.C., Gallant, D., Hall, J.K., Hehemann, L., Hodnesdal, H., Hong, J., Ivaldi, R., Kane, E., Klaucke, I., Krawczyk, D.W., Kristoffersen, Y., Kuipers, B.R., Millan, R., Masetti, G., Morlighem, M., Noormets, R., Prescott, M.M., Rebesco, M., Rignot, E., Semiletov, I., Tate, A.J., Travaglini, P., Velicogna, I., Weatherall, P., Weinrebe, W., Willis, J.K., Wood, M., Zarayskaya, Y., Zhang, T., Zimmermann, M., Zinglersen, K.B., 2020. The international bathymetric chart of the Arctic ocean version 4.0. Sci. Data 7, 1–14. https://doi.org/10.1038/s41597-020-0520-9.
Jennings, A.E., Knudsen, K.L., Hald, M., Hansen, C.V., Andrews, J.T., 2002. A mid-Holocene shift in Arctic sea-ice variability on the East Greenland Shelf. Holocene 12, 49–58. https://doi.org/10.1191/0959683602hl519rp.
Jennings, A.E., Walton, M.E., Ó Cofaigh, C., Kilfeather, A., Andrews, J.T., Ortiz, J.D., de Vernal, A., Dowdeswell, J.A., 2014. Paleoenvironments during younger dryas-early Holocene retreat of the Greenland ice sheet from outer disko trough, central west Greenland. J. Quat. Sci. 29, 27–40. https://doi.org/10.1002/jqs.2652.
Johannessen, O.M., Khvorostovsky, K., Miles, M.W., Bobylev, L.P., 2005. Recent ice-sheet growth in the interior of Greenland. Science 310, 1013–1016. https://doi.org/10.1126/science.1115356.
Jonkers, L., Barker, S., Hall, I.R., Prins, M.A., 2015. Correcting for the influence of ice-rafted detritus on grain size-based paleocurrent speed estimates. Paleoceanography 30, 1347–1357. https://doi.org/10.1002/2015PA002830.
Kaufman, D.S., Ager, T.A., Anderson, N.J., Anderson, P.M., Andrews, J.T., Bartlein, P.J., Brubaker, L.B., Coats, L.L., Cwynar, L.C., Duvall, M.L., Dyke, A.S., Edwards, M.E., Eisner, W.R., Gajewski, K., Geirsdóttir, A., Hu, F.S., Jennings, A.E., Kaplan, M.R., Kerwin, M.W., Lozhkin, A.V., MacDonald, G.M., Miller, G.H., Mock, C.J., Oswald, W.W., Otto-Bliesner, B.L., Porinchu, D.F., Rühland, K., Smol, J.P., Steig, E.J., Wolfe, B.B., 2004. Holocene thermal maximum in the western Arctic (0-180°W). Quat. Sci. Rev. 23, 529–560. https://doi.org/10.1016/j.quascirev.2003.09.007.
Kleiven, H.K.F., Ninnemann, U.S., Kissel, C., Laj, C., Cortijo, E., Richter, T.O., 2008. Reduced North Atlantic deep water coeval with the glacial lake Agassiz freshwater outburst. Science 319, 60–64. https://doi.org/10.1126/science.1148924.
Klinck, J.M., 1996. Circulation near submarine canyons: a modeling study. J. Geophys. Res. C Oceans 101, 1211–1223. https://doi.org/10.1029/95JC02901.
Koç, N., Jansen, E., Hald, M., Labeyrie, L., 1996. Late glacial-holocene sea surface temperatures and gradients between the north Atlantic and the Norwegian sea: implications for the nordic heat pump. Geol. Soc. Spec. Publ. https://doi.org/10.1144/GSL.SP.1996.111.01.12.
Kuhlbrodt, T., Griesel, A., Montoya, M., Levermann, A., Hofmann, M., Rahmstorf, S., 2007. On the driving processes of the Atlantic meridional overturning circulation. Rev. Geophys. 45, RG2001 https://doi.org/10.1029/2004RG000166.
Langner, M., Mulitza, S., 2019. Technical note: PaleoDataView - a software toolbox for the collection, homogenization and visualization of marine proxy data. Clim. Past 15, 2067–2072. https://doi.org/10.5194/cp-15-2067-2019.
Larsen, N.K., Funder, S.V., Kjær, K.H., Kjeldsen, K.K., Knudsen, M.F., Linge, H., 2014. Rapid early Holocene ice retreat in West Greenland. Quat. Sci. Rev. 92, 310–323. https://doi.org/10.1016/j.quascirev.2013.05.027.
Larsen, N.K., Kjær, K.H., Lecavalier, B.S., Bjørk, A.A., Colding, S., Huybrechts, P., Jakobsen, K.E., Kjeldsen, K.K., Knudsen, K.L., Odgaard, B.V., Olsen, J., 2015. The response of the southern Greenland ice sheet to the Holocene thermal maximum. Geology 43, 291–294. https://doi.org/10.1130/G36476.1.
Lecavalier, B.S., Milne, G.A., Simpson, M.J.R.R., Wake, L., Huybrechts, P., Tarasov, L., Kjeldsen, K.K., Funder, S., Long, A.J., Woodroffe, S., Dyke, A.S., Larsen, N.K., 2014. A model of Greenland ice sheet deglaciation constrained by observations of relative sea level and ice extent. Quat. Sci. Rev. 102, 54–84. https://doi.org/10.1016/j.quascirev.2014.07.018.
Leng, W., von Dobeneck, T., Bergmann, F., Just, J., Mulitza, S., Chiessi, C.M., St-Onge, G., Piper, D.J.W., 2018. Sedimentary and rock magnetic signatures and event scenarios of deglacial outburst floods from the Laurentian Channel Ice Stream. Quat. Sci. Rev. 186, 27–46. https://doi.org/10.1016/j.quascirev.2018.01.016.
Li, D., Sha, L., Li, J., Jiang, H., Liu, Y., Wu, Y., 2017. Summer sea-surface temperatures and climatic events in Vaigat Strait, West Greenland, during the last 5000 years. Sustain. Times 9, 1–16. https://doi.org/10.3390/su9050704.
Lochte, A.A., Repschläger, J., Seidenkrantz, M.-S., Kienast, M., Blanz, T., Schneider, R.R., 2019. Holocene water mass changes in the Labrador Current. Holocene 29, 676–690. https://doi.org/10.1177/0959683618824752.
Lyle, M., Lyle, A.O., Gorgas, T., Holbourn, A., Westerhold, T., Hathorne, E.C., Kimoto, K., Yamamoto, S., 2012. Data report : raw and normalized elemental data along the Site U1338 splice from X-ray fluorescence scanning. Proc. Integr. Ocean Drill. Program 320/321 320, 1–19. https://doi.org/10.2204/iodp.proc.320321.203.2012.
Lynch-Stieglitz, J., Adkins, J.F., Curry, W.B., Dokken, T.M., Hall, I.R., Herguera, J.C., Hirschi Ivanova, E.V., Kissel, C., Marchal, O., Marchitto, T.M., McCave, I.N., McManus, J.F., Mulitza, S., Ninnemann, U., Peeters, F., Yu, E.-F., Zahn, R., 2007. Atlantic meridional overturning circulation during the last glacial maximum. Science 316, 66–69. https://doi.org/10.1126/science.1137127.
Marchès, E., Mulder, T., Cremer, M., Bonnel, C., Hanquiez, V., Gonthier, E., Lecroart, P., 2007. Contourite drift construction influenced by capture of Mediterranean Outflow Water deep-sea current by the Portimão submarine canyon (Gulf of Cadiz, South Portugal). Mar. Geol. 242, 247–260. https://doi.org/10.1016/j.margeo.2007.03.013.
McCave, I.N., Andrews, J.T., 2019a. Distinguishing current effects in sediments delivered to the ocean by ice. II. Glacial to Holocene changes in high latitude North Atlantic upper ocean flows. Quat. Sci. Rev. 223, 105902. https://doi.org/10.1016/j.quascirev.2019.105902.
McCave, I.N., Andrews, J.T., 2019b. Distinguishing current effects in sediments delivered to the ocean by ice. I. Principles, methods and examples. Quat. Sci. Rev. 212, 92–107. https://doi.org/10.1016/j.quascirev.2019.03.031.
McCave, I.N., Hall, I.R., 2006. Size sorting in marine muds: processes, pitfalls, and prospects for paleoflow-speed proxies. Geochem. Geophys. Geosyst. 7 https://doi.org/10.1029/2006GC001284.
McCave, I.N., Manighetti, B., Robinson, S.G., 1995. Sortable silt and fine sediment size/composition slicing: parameters for palaeocurrent speed and palaeoceanography. Paleoceanography 10, 593–610. https://doi.org/10.1029/94PA03039.
McCave, I.N., Thornalley, D.J.R., Hall, I.R., 2017. Relation of sortable silt grain size to deep-sea current speeds: calibration of the "Mud Current Meter. Deep. Res. Part I. https://doi.org/10.1016/j.dsr.2017.07.003.
McGregor, H.V., Dupont, L., Stuut, J.B.W., Kuhlmann, H., 2009. Vegetation change, goats, and religion: a 2000-year history of land use in southern Morocco. Quat. Sci. Rev. 28, 1434–1448. https://doi.org/10.1016/j.quascirev.2009.02.012.
Møller, H.S., Jensen, K.G., Kuijpers, A., Aagaard-Sørensen, S., Seidenkrantz, M.-S., Prins, M., Endler, R., Mikkelsen, N., 2006. Late-Holocene environment and climatic changes in Ameralik Fjord, southwest Greenland: evidence from the sedimentary record. Holocene 16, 685–695. https://doi.org/10.1191/0959683606hl963rp.
Morlighem, M., Williams, C.N., Rignot, E., An, L., Arndt, J.E., Bamber, J.L., Catania, G.A., Chauché, N., Dowdeswell, J.A., Dorschel, B., Fenty, I., Hogan, K., Howat, I., Hubbard, A., Jakobsson, M., Jordan, T.M., Kjeldsen, K.K., Millan, R., Mayer, L., Mouginot, J., Noël, B.P.Y., O Cofaigh, C., Palmer, S., Rysgaard, S., Seroussi, H., Siegert, M.J., Slabon, P., Straneo, F., van den Broeke, M.R., Weinrebe, W., Wood, M., Zinglersen, K.B., 2017. BedMachine v3: complete bed topography and ocean bathymetry mapping of Greenland from multibeam echo sounding combined with mass conservation. Geophys. Res. Lett. 44 (11) https://doi.org/10.1002/2017GL074954, 051-11,061.
Moros, M., Lloyd, J.M., Perner, K., Krawczyk, D.W., Blanz, T., de Vernal, A., Ouellet-Bernier, M.M., Kuijpers, A., Jennings, A.E., Witkowski, A., Schneider, R.R., Jansen, E., 2016. Surface and sub-surface multi-proxy reconstruction of middle to late Holocene palaeoceanographic changes in Disko Bugt, West Greenland. Quat. Sci. Rev. 132, 146–160. https://doi.org/10.1016/j.quascirev.2015.11.017.
Mulder, T., Syvitski, J.P.M., 1995. Turbidity currents generated at river mouths during exceptional discharges to the world oceans. J. Geol. 103, 285–299.
Mulder, T., Syvitski, J.P.M.M., Migeon, S., Faugères, J.C., Savoye, B., 2003. Marine hyperpycnal flows: initiation, behaviorand related deposits. A review. Mar. Petrol. Geol. 20, 861–882. https://doi.org/10.1016/j.marpetgeo.2003.01.003.
Myers, P.G., Kulan, N., Ribergaard, M.H., 2007. Irminger water variability in the west Greenland current. Geophys. Res. Lett. 34, 2–7. https://doi.org/10.1029/2007GL030419.
Ó Cofaigh, C., Dowdeswell, J.A., Jennings, A.E., Hogan, K.A., Kilfeather, A.A., Hiemstra, J.F., Noormets, R., Evans, J.R., McCarthy, D.J., Andrews, J.T., Lloyd, J.M., Moros, M., O Cofaigh, C., 2013. An extensive and dynamic ice sheet on the west Greenland shelf during the last glacial cycle. Geology 41, 219–222. https://doi.org/10.1130/G33759.1.
Ólafsdóttir, S., Jennings, A.E., Geirsdóttir, Á., Andrews, J.T., Miller, G.H., 2010. Holocene variability of the North Atlantic Irminger current on the south- and northwest shelf of Iceland. Mar. Micropaleontol. 77, 101–118. https://doi.org/10.1016/j.marmicro.2010.08.002.
Ouellet-Bernier, M.-M.M., de Vernal, A., Hillaire-Marcel, C., Moros, M., 2014. Paleoceanographic changes in the disko bugt area, west Greenland, during the Holocene. Holocene 24, 1573–1583. https://doi.org/10.1177/0959683614544060.
Parsons, J.D., Bush, J.W.M., Syvitski, J.P.M., 2001. Hyperpycnal plume formation from riverine outflows with small sediment concentrations. Sedimentology 48, 465–478. https://doi.org/10.1046/j.1365-3091.2001.00384.x.
Paterson, G.A., Heslop, D., 2015. New methods for unmixing sediment grain size data. Geochem. Geophys. Geosyst. 16, 4494–4506. https://doi.org/10.1002/2015GC006070.
Peltier, W.R., Fairbanks, R.G., 2006. Global glacial ice volume and Last Glacial Maximum duration from an extended Barbados sea level record. Quat. Sci. Rev. 25, 3322–3337. https://doi.org/10.1016/j.quascirev.2006.04.010.
Perner, K., Moros, M., Jennings, A.E., Lloyd, J.M., Knudsen, K.L., 2013. Holocene palaeoceanographic evolution off West Greenland. Holocene 23, 374–387. https://doi.org/10.1177/0959683612460785.
Praetorius, S.K., McManus, J.F., Oppo, D.W., Curry, W.B., 2008. Episodic reductions in bottom-water currents since the last ice age. Nat. Geosci. 1, 449–452. https://doi.org/10.1038/ngeo227.
Rahmstorf, S., 1996. On the freshwater forcing and transport of the Atlantic thermohaline circulation. Clim. Dynam. 12, 799–811. https://doi.org/10.1007/s003820050144.
Rahmstorf, S., Crucifix, M., Ganopolski, A., Goosse, H., Kamenkovich, I., Knutti, R., Lohmann, G., Marsh, R., Mysak, L.A., Wang, Z., Weaver, A.J., Myzak, L.A., Wang, Z., Weaver, A.J., 2005. Thermohaline circulation hysteresis: a model intercomparison. Geophys. Res. Lett. 32, 1–5. https://doi.org/10.1029/2005GL023655.

Rasch, M., Elberling, B., Jakobsen, B.H., Hasholt, B., 2000. High-resolution measurements of water discharge, sediment, and solute transport in the river zackenbergelven, northeast Greenland. Arctic Antarct. Alpine Res. 32, 336–345.
Reimer, P.J., Bard, E., Bayliss, A., Beck, J.W., Blackwell, P.G., Ramsey, C.B., Buck, C.E., Cheng, H., Edwards, R.L., Friedrich, M., Grootes, P.M., Guilderson, T.P., Haflidason, H., Hajdas, I., Hatté, C., Heaton, T.J., Hoffmann, D.L., Hogg, A.G., Hughen, K.A., Kaiser, K.F., Kromer, B., Manning, S.W., Niu, M., Reimer, R.W., Richards, D.A., Scott, E.M., Southon, J.R., Staff, R.A., Turney, C.S.M., van der Plicht, J., Bronk Ramsey, C., 2013. IntCal13 and Marine13 radiocarbon age calibration curves 0–50,000 Years cal BP. Radiocarbon 55, 1869–1887. https://doi.org/10.2458/azu_js_rc.55.16947.
Ren, J., Jiang, H., Seidenkrantz, M.S., Kuijpers, A., 2009. A diatom-based reconstruction of Early Holocene hydrographic and climatic change in a southwest Greenland fjord. Mar. Micropaleontol. 70, 166–176. https://doi.org/10.1016/j.marmicro.2008.12.003.
Renssen, H., Goosse, H., Fichefet, T., Campin, J.M., 2001. The 8.2 kyr BP event simulated by a global atmosphere-sea-ice-ocean model. Geophys. Res. Lett. 28, 1567–1570. https://doi.org/10.1029/2000GL012602.
Reusche, M., Winsor, K., Carlson, A.E., Marcott, S.A., Rood, D.H., Novak, A., Roof, S.R., Retelle, M., Werner, A., Caffee, M.W., Clark, P.U., 2014. 10Be surface exposure ages on the late-Pleistocene and Holocene history of Linnébreen on Svalbard. Quat. Sci. Rev. 89, 5–12. https://doi.org/10.1016/j.quascirev.2014.01.017.
Ribergaard, M.H., 2014. Oceanographic investigations off West Greenland 2013. Danish Meteorol. Inst. Cent. Ocean Ice 49.
Ritz, S.P., Stocker, T.F., Grimalt, J.O., Menviel, L., Timmermann, A., 2013. Estimated strength of the Atlantic overturning circulation during the last deglaciation. Nat. Geosci. 6, 208–212. https://doi.org/10.1038/ngeo1723.
Saini, J., Stein, R., Fahl, K., Weiser, J., Hebbeln, D., Hillaire-Marcel, C., de Vernal, A., 2020. Holocene Variability in Sea Ice and Primary Productivity in the Northeastern Baffin Bay. arktos, pp. 1–19. https://doi.org/10.1007/s41063-020-00075-y.
Schmittner, A., 2005. Decline of the marine ecosystem caused by a reduction in the Atlantic overturning circulation. Nature 434, 628–633. https://doi.org/10.1038/nature03476.
Schweinsberg, A.D., Briner, J.P., Miller, G.H., Bennike, O., Thomas, E.K., 2017. Local glaciation in west Greenland linked to North Atlantic ocean circulation during the Holocene. Geology 45, G38114. https://doi.org/10.1130/G38114.1.
Secher, K., 1980. Distribution of radioactive mineralisation in central West Greenland. Rapp. Grønlands Geol. Undersøgelse 100, 61–65.
Seidenkrantz, M.-S., 2013. Benthic foraminifera as palaeo sea-ice indicators in the subarctic realm - examples from the Labrador Sea-Baffin Bay region. Quat. Sci. Rev. 79, 135–144. https://doi.org/10.1016/j.quascirev.2013.03.014.
Seidenkrantz, M.-S.S., Ebbesen, H., Aagaard-Sørensen, S., Moros, M., Lloyd, J.M., Olsen, J., Knudsen, M.F., Kuijpers, A., Faurschou, M., Kuijpers, A., 2013. Early Holocene large-scale meltwater discharge from Greenland documented by foraminifera and sediment parameters. Palaeogeogr. Palaeoclimatol. Palaeoecol. 391, 71–81. https://doi.org/10.1016/j.palaeo.2012.04.006.
Slabon, P., Dorschel, B., Jokat, W., Myklebust, R., Hebbeln, D., Gebhardt, A.C., 2016. Greenland ice sheet retreat history in the northeast Baffin Bay based on high-resolution bathymetry. Quat. Sci. Rev. 154, 182–198. https://doi.org/10.1016/j.quascirev.2016.10.022.
Solignac, S., De Vernal, A., Hillaire-Marcel, C., 2004. Holocene sea-surface conditions in the North Atlantic - contrasted trends and regimes in the western and eastern sectors (Labrador Sea vs. Iceland Basin). Quat. Sci. Rev. 23, 319–334. https://doi.org/10.1016/j.quascirev.2003.06.003.
Stein, R., 2008. Arctic Ocean Sediments: Processes, Proxies and Paleoenvironments. In: Developments in Marine Geology, first ed. Elsevier. https://doi.org/10.1016/S1572-5480(08)00002-X.
Szczuciński, W., Zajączkowski, M., 2013. Factors controlling downward fluxes of particulate matter in glacier-contact and non-glacier contact settings in a subpolar fjord (billefjorden, svalbard). Sediments, morphol. Sediment. Process. Cont. Shelves 369–386. https://doi.org/10.1002/9781118311172.ch18.
Tang, C.C.L., Ross, C.K., Yao, T., Petrie, B., DeTracey, B.M., Dunlap, E., 2004. The circulation, water masses and sea-ice of Baffin Bay. Prog. Oceanogr. 63, 183–228. https://doi.org/10.1016/j.pocean.2004.09.005.
Teller, J.T., Leverington, D.W., 2004. Glacial Lake Agassiz: a 5000 yr history of change and its relationship to the δ18O record of Greenland. Bull. Geol. Soc. Am. 116, 729–742. https://doi.org/10.1130/B25316.1.
Thornalley, D.J.R., Blaschek, M., Davies, F.J., Praetorius, S.K., Oppo, D.W., McManus, J.F., Hall, I.R., Kleiven, H.K.F., Renssen, H., McCave, I.N., 2013. Long-term variations in Iceland-Scotland overflow strength during the Holocene. Clim. Past 9, 2073–2084. https://doi.org/10.5194/cp-9-2073-2013.
Thornalley, D.J.R., Elderfield, H., McCave, I.N., 2010. Intermediate and deep water paleoceanography of the northern North Atlantic over the past 21,000 years. Paleoceanography 25, 1–17. https://doi.org/10.1029/2009PA001833.
Thornalley, D.J.R., Oppo, D.W., Ortega, P., Robson, J.I., Brierley, C.M., Davis, R., Hall, I.R., Moffa-Sanchez, P., Rose, N.L., Spooner, P.T., Yashayaev, I., Keigwin, L.D., 2018. Anomalously weak Labrador Sea convection and Atlantic overturning during the past 150 years. Nature 556, 227–230. https://doi.org/10.1038/s41586-018-0007-4.
Tjallingii, R., Röhl, U., Kölling, M., Bickert, T., 2007. Influence of the water content on X-ray fluorescence core scanning measurements in soft marine sediments. Geochem. Geophys. Geosyst. 8, 1–12. https://doi.org/10.1029/2006GC001393.
van Hateren, J.A., Prins, M.A., van Balen, R.T., 2018. On the genetically meaningful decomposition of grain-size distributions: a comparison of different end-member modelling algorithms. Sediment. Geol. 375, 49–71. https://doi.org/10.1016/j.sedgeo.2017.12.003.
Vinther, B.M., Buchardt, S.L., Clausen, H.B., Dahl-Jensen, D., Johnsen, S.J., Fisher, D.A., Koerner, R.M., Raynaud, D., Lipenkov, V., Andersen, K.K., Blunier, T., Rasmussen, S.O., Steffensen, J.P., Svensson, A.M., 2009. Holocene thinning of the Greenland ice sheet. Nature 461, 385–388. https://doi.org/10.1038/nature08355.
Voigt, I., Henrich, R., Preu, B.M., Piola, A.R., Hanebuth, T.J.J., Schwenk, T., Chiessi, C.M., 2013. A submarine canyon as a climate archive - interaction of the Antarctic intermediate water with the Mar del Plata canyon (southwest Atlantic). Mar. Geol. 341, 46–57. https://doi.org/10.1016/j.margeo.2013.05.002.
Wacker, L., Fülöp, R.H., Hajdas, I., Molnár, M., Rethemeyer, J., 2013. A novel approach to process carbonate samples for radiocarbon measurements with helium carrier gas. Nucl. Instrum. Methods Phys. Res. Sect. B Beam Interact. Mater. Atoms 294, 214–217. https://doi.org/10.1016/j.nimb.2012.08.030.
Weidick, A., Bennike, O., Citterio, M., Nørgaard-Pedersen, N., 2012. Neoglacial and historical glacier changes around Kangersuneq fjord in southern West Greenland. Geol. Surv. Den. Greenl. Bull.
Weijer, W., Maltrud, M.E., Hecht, M.W., Dijkstra, H.A., Kliphuis, M.A., 2012. Response of the Atlantic Ocean circulation to Greenland Ice Sheet melting in a strongly-eddying ocean model. Geophys. Res. Lett. 39, 1–6. https://doi.org/10.1029/2012GL051611.
Weltje, G.J., Tjallingii, R., 2008. Calibration of XRF core scanners for quantitative geochemical logging of sediment cores: theory and application. Earth Planet Sci. Lett. 274, 423–438. https://doi.org/10.1016/j.epsl.2008.07.054.
Wright, L.D., 2012. Recent advances in understanding continental shelf sediment transport. Int. Assoc. Sedimentol. Spec. Publ. 44, 159–172.
Wright, L.D., Friedrichs, C.T., Scully, M.E., 2002. Pulsational gravity-driven sediment transport on two energetic shelves. Continent. Shelf Res. 22, 2443–2460. https://doi.org/10.1016/S0278-4343(02)00133-4.
Wu, L., Wang, R., Xiao, W., Krijgsman, W., Li, Q., Ge, S., Ma, T., 2018. Late quaternary deep stratification-climate coupling in the southern ocean: implications for changes in Abyssal carbon storage. Geochem. Geophys. Geosyst. 19, 379–395. https://doi.org/10.1002/2017GC007250.
Yashayaev, I., 2007. Hydrographic changes in the Labrador Sea, 1960-2005. Prog. Oceanogr. 73, 242–276. https://doi.org/10.1016/j.pocean.2007.04.015.
Young, N.E., Briner, J.P., 2015. Holocene evolution of the western Greenland Ice Sheet: Assessing geophysical ice-sheet models with geological reconstructions of ice-margin change. Quat. Sci. Rev. 114, 1–17. https://doi.org/10.1016/j.quascirev.2015.01.018.